# Ocean floor and subduction record in the Zermatt-Saas rodingites, Valtournanche, Western Alps

D. ZANONI,[1] G. REBAY[2] AND M. I. SPALLA[1]
[1]Dipartimento di Scienze della Terra "A. Desio", Università degli Studi di Milano, Via Mangiagalli 34, 20133, Milan, Italy (davide.zanoni@unimi.it)
[2]Dipartimento di Scienze della Terra e dell'Ambiente, Università degli Studi di Pavia, Via Ferrata 1, 27100 Pavia, Italy

ABSTRACT Multiscale structural analysis and petrological modelling were used to establish the pressure-peak mineral assemblages and pressure–temperature (P–T) conditions recorded in the rodingites of the upper Valtournanche portion of the oceanic Zermatt-Saas Zone (ZSZ; Western Alps, northwestern Italy) during Alpine subduction. Rodingites occur in the form of deformed dykes and boudins within the hosting serpentinites. A field structural analysis showed that rodingites and serpentinites record four ductile deformation stages (D1–D4) during the Alpine cycle, with the first three stages associated with new foliations. The most pervasive fabric is S2 that is marked by mineral assemblages in serpentinite indicating pressure-peak conditions, involving mostly serpentine, clinopyroxene, olivine, Ti-clinohumite and chlorite. Three rodingite types can be defined: epidote-bearing, garnet– chlorite–clinopyroxene-bearing and vesuvianite-bearing rodingite. In these, the pressure-peak assem- blages coeval with S2 development involve: (i) epidote$_{II}$ + clinopyroxene$_{II}$ + Mg-chlorite$_{II}$ + garnet$_{II}$ ± rutile ± tremolite$_{I}$ in the epidote-bearing rodingite; (ii) Mg-chlorite$_{II}$ + garnet$_{II}$ clinopy- roxene$_{II}$ ± vesuvianite$_{II}$ ± ilmenite in the garnet–chlorite–clinopyroxene-bearing rodingite; (iii) vesuvianite$_{II}$ + Mg-chlorite$_{II}$ + clinopyroxene$_{II}$ + garnet$_{II}$± rutile ± epidote in vesuvianite-bearing rodingite. Despite the pervasive structural reworking of the rodingites during Alpine subduction, the mineral relicts of the pre-Alpine ocean floor history have been preserved and consist of clinopyroxene porphyroclasts (probable igneous relicts from gabbro dykes) and Cr-rich garnet and vesuvianite (relicts of ocean floor metasomatism). Petrological modelling using THERMOCALC in the NCFMASHTO system was used to constrain the P–T conditions of the S2 mineral assemblages. The inferred values of 2.3–2.8 GPa and 580–660 °C are consistent with those obtained for syn-S2 assemblages in the surrounding serpentinites. Multiscale structural analysis indicates that some ocean floor minerals remained stable under eclogite facies conditions suggesting that minerals such as vesuvianite, which is generally regarded as a low-P phase, could also be stable in favourable chemical systems under high-P/ultra-high-pressure (HP/UHP) conditions. Finally, the reconstructed P–T–d–t path indicates that the P/T ratio characterizing the D2 stage is consistent with cold subduction as estimated in this part of the Alps. The estimated pressure-peak values are higher than those previously reported in this part of ZSZ, suggesting that the UHP units are larger and/or more abundant than those previously suggested.

Key words: Alpine subduction; eclogitized rodingite; HP/UHP vesuvianite; tectono-metamorphic evolution; Tethys ocean.

## INTRODUCTION

The Zermatt-Saas Zone (ZSZ) ophiolitic complex, which outcrops in the upper Valtournanche (Val d'Aosta, northwestern Italy), consists of high-pressure/ultra-high-pressure (HP/UHP) metaophiolites in which the petrological and structural evolution of metagabbros, metabasalts and serpentinites can be constrained (e.g. Ernst & Dal Piaz, 1978; Dal Piaz et al., 1980; Barnicoat & Fry, 1986; Bucher et al., 2005; Angiboust et al., 2009; Bucher & Grapes, 2009; Groppo et al., 2009; Ferrando et al., 2010; Rebay et al., 2012; Zanoni et al., 2012). The deformation–metamorphism relationships in rodingites have been partly overlooked because of their complex composition and mineralogy (Zanoni et al., 2012). Quantitative petrological analysis has investigated factors that control the development of metasomatic reactions but have left unresolved questions regarding the relative timing of formation of the rodingites, which could have occurred anywhere along the P–T path from ocean floor to subduction and subsequent exhumation (e.g. Scambelluri & Rampone, 1999; Li et al., 2008; Ferrando et al., 2010). To identify the structural and metamorphic features characteristic of oceanic and subduction environments in rodingites,

the results of structural analysis of superposed fabrics (e.g. Turner & Weiss, 1963; Pitcher & Flinn, 1965; Williams, 1985; Spalla et al., 2005; Hobbs et al., 2010; Gosso et al., 2015) integrated with detailed petrological studies and supported by thermodynamic modelling (e.g. THERMOCALC, Powell et al., 1998), are examined. In addition, complex chemical systems such as those of rodingites that record a polyphase structural history, as indicated by boudins and transposed dykes in the ZSZ HP/UHP serpentinites (Rahn & Bucher, 1998; Li et al., 2004a,b, 2008; Ferrando et al., 2010; Rebay et al., 2012; Zanoni et al., 2012), can be the Ariadne thread to differentiate the oceanic and subduction–collision imprints using rodingite mineralogical and structural memory.

Rodingites are Si-undersaturated and Ca-rich rocks derived from metasomatic reactions between peridotites and gabbro-basalt dykes and generally form at the ocean floor (e.g. Nicolas, 1966; Coleman, 1967; Honnorez & Kirst, 1975; O'Hanley et al., 1992; Palandri & Reed, 2004; Austrheim & Prestvik, 2008; Frost et al., 2008; Bach & Klein, 2009). Nevertheless, rodingites from various collisional belts have been interpreted as having re-crystallized or formed during the subduction or exhumation of eclogitic rocks, although a detailed description of the mineral assemblages defining successive fabrics and related mineral compositional variations has not generally been reported (Dal Piaz, 1967; Piccardo et al., 1980; Puga et al., 1999; Li et al., 2007, 2008; Tsikouras et al., 2009; Ferrando et al., 2010). Furthermore, rodingitization in involving Na-depletion, which may also continue during subduction and exhumation, obscures the effect of eclogitic metamorphism in rodingites. Among rodingite-forming minerals, vesuvianite is commonly considered a low-grade metamorphic mineral, but recently it was found in jadeitites from Myanmar and has been described as belonging to HP metamorphic assemblages in ZSZ eclogitized rodingites (Li et al., 2008; Nyunt et al., 2009; Zanoni et al., 2012).

In this study, a structural continuous correlation was first applied during field investigation, and a microscale deformation–metamorphism analysis was then conducted for identifying HP/UHP equilibrium mineral assemblages associated with Alpine fabrics in different rodingite types. In addition, a structural correlation between foliations supported by the HP/UHP assemblages and contemporaneous fabrics in the surrounding serpentinite, for which the P–T conditions were previously determined (Rebay et al., 2012), was used to benchmark the estimates of climax conditions in the rodingites. Correlating the deformation–metamorphism relationships that developed under varying conditions in rodingite and surrounding rocks, from low pressure to HP/UHP, such as vesuvianite compositional differences found in different microstructural sites, facilitated the identification of pre-Alpine rodingite relict occurrences. Petrological modelling was only possible for rodingites with parageneses that consist of thermodynamically constrained phases, like clinopyroxene, garnet, epidote and chlorite. The results provide new insights to supplement the limited available petrological work, which primarily focused on the contact metamorphism zone and P–T fields at pressures lower than 1 GPa (e.g. Frost, 1975; Rice, 1983; Castelli et al., 1995).

## GEOLOGICAL SETTING

The ZSZ outcrops in the western Alps and consists of rocks derived from the Piedmont–Ligurian oceanic lithosphere (Fig. 1a,b) that are dominated by subduction-related Alpine eclogite facies imprints, locally re-equilibrated under exhumation-related greenschist facies metamorphism (e.g. Ernst & Dal Piaz, 1978; Cartwright & Barnicoat, 2002; McNamara et al., 2012; Lardeaux, 2014). The ZSZ, together with the Combin Zone (CZ), forms the oceanic suture of the Western European Alps (e.g. Caron et al., 1984; Reddy et al., 1999; Spalla et al., 2010 and references therein).

Within the Alpine nappe pile, the ZSZ and the CZ are tectonically sandwiched between the continental Penninic Monte Rosa and the Austroalpine Dent Blanche–Sesia Lanzo nappe system (e.g. Bearth, 1967; Polino et al., 1990; Handy et al., 2010), and they are separated by the Pancherot-Cime Bianche unit, which consists of rocks primarily derived from Permian to Cretaceous sediments (Dal Piaz, 1999). The CZ is considered as derived from the ocean–continent transition zone and is structurally shallower than ZSZ (e.g. Dal Piaz & Ernst, 1978; Dal Piaz et al., 1981). Recently, some ophiolitic complexes of the Western Alps have been interpreted as oceanic core complexes characteristic of slow-spreading oceanic ridges (Festa et al., 2015; Lagabrielle et al., 2015).

Compared with the ZSZ, the CZ is affected by pervasive greenschist facies re-equilibration, but preserves some blueschist facies relicts (Dal Piaz, 1974; Dal Piaz & Ernst, 1978; Ring, 1995; Cartwright & Barnicoat, 2002). The contact between the ZSZ and the CZ has been interpreted as a detachment fault reactivated by a thrust fault (Ballèvre & Merle, 1993) or as a thrust fault reactivated by a normal fault (Pleuger et al., 2007).

The ZSZ consists of serpentinites, metagabbros and N-MORB metabasalts with minor pelagic metasedimentary rocks (Dal Piaz et al., 1981; Beccaluva et al., 1984; Pfeiffer et al., 1989; Martin et al., 1994; Dale et al., 2009; Wassmann et al., 2011; Rebay et al., 2012). Metasedimentary rocks are primarily calcschists and quartzites that were either derived from the internal portion of the oceanic realm (e.g. Bearth, 1967; Ernst & Dal Piaz, 1978), or deposited on continental shelves, continental slopes, or marine basins (Mahlen et al., 2005). The pre-

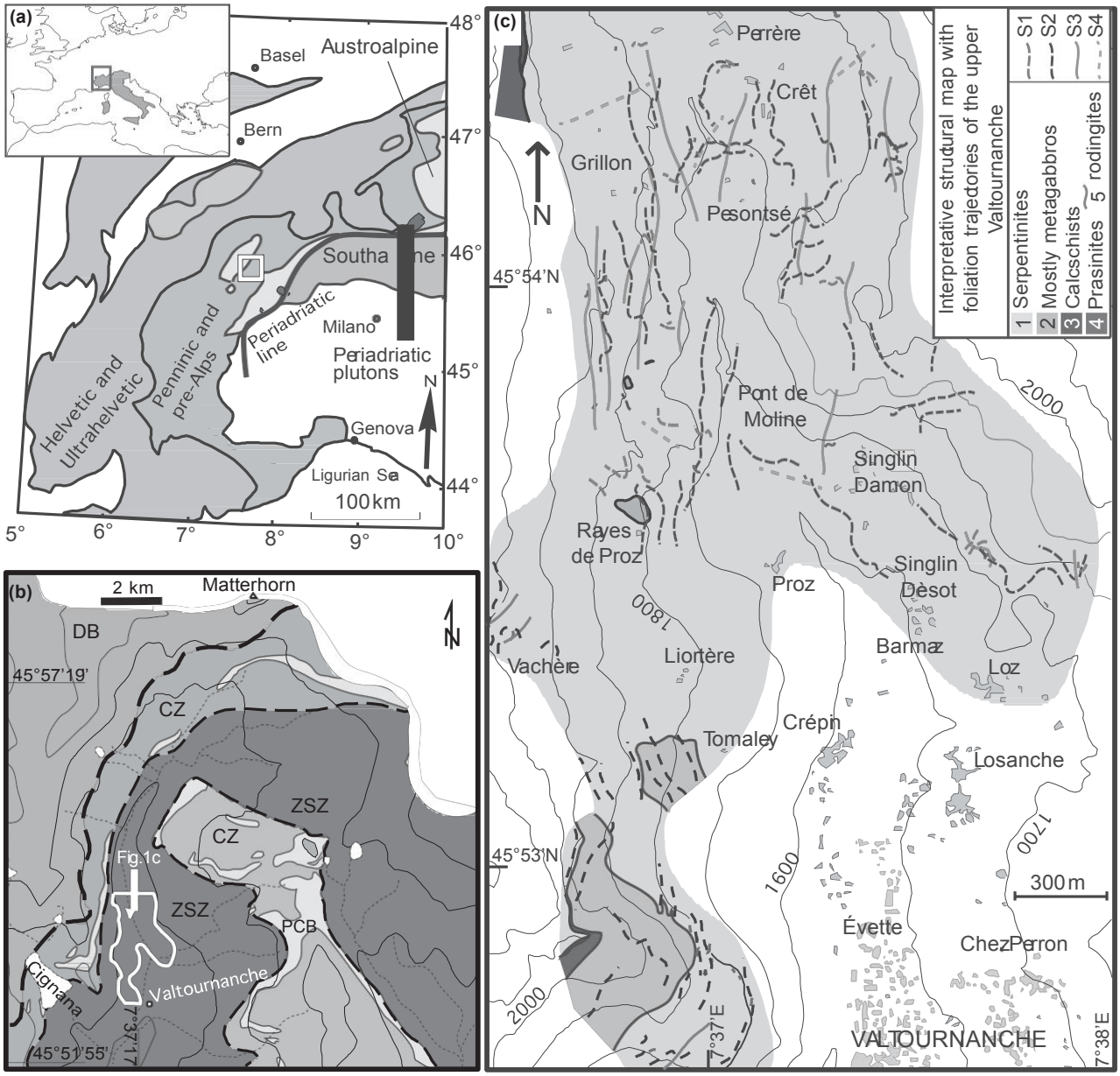


Fig. 1. Geological and structural setting of the upper Valtournanche. (a) Tectonic sketch map of the Western Alps and its location within Europe and the Mediterranean region. (b) Interpretative tectonic sketch of the upper Valtournanche redrawn from the geotectonic map of the Aosta Valley (De Giusti et al., 2003); area indicated by the thick white square in (a). ZSZ, Zermatt-Saas Zone; PCB, Pancherot-Cime Bianche unit; CZ, Combin Zone; DB, Dent Blanche nappe. (c) Interpretative structural map, modified after Zanoni et al. (2012), with the foliation trajectories and lithostratigraphy of the meta-ophiolites of the upper Valtournanche (ZSZ); map indicated by the thick white line in (b). Relative chronology of superposed foliation is shown in the legend. Topography redrawn from the technical map of the Val d'Aosta Regional Administration without hydrography.

Alpine structural and mineral relicts that preserve oceanic textures (Barnicoat & Fry, 1986; Martin & Tartarotti, 1989; Fontana et al., 2008, 2015; Rebay et al., 2012), dated between 164 and 153 Ma (Rubatto, 1998), show that the ZSZ lithosphere was affected by oceanic metamorphism prior to Alpine subduction (Bearth, 1976; Dal Piaz et al., 1980; Li et al., 2004b). During the Alpine subduction, the ZSZ recorded a blueschist facies metamorphic imprint that predates the eclogite peak (e.g. Chinner & Dixon, 1973; Ernst & Dal Piaz, 1978). Petrological investigations of the ZSZ metabasic rocks indicate the following peak conditions: 2.5–3.0 GPa and 550–600 °C (Bucher et al., 2005), 1.9–2.2 GPa and 530–600 °C (Dale et al., 2009) and, south of the Aosta-Ranzola fault (St. Marcel valley), 2.1 ± 0.3 GPa and 550 ± 60 °C (Martin et al., 2008). The metagabbros of the Swiss portion of the ZSZ record

peak conditions of 2.5–2.8 GPa and 600–610 °C (Bucher & Grapes, 2009) or alternatively 1.9–2.2 GPa for 500–580 °C (Dale et al., 2009). Pressures from 2.7 to over 3.2 GPa and temperatures of 590–630 °C are estimated at Lago di Cignana (e.g. Reinecke, 1991, 1998; van der Klauw et al., 1997; Groppo et al., 2009), where microdiamond has also been found in oceanic metasedimentary rocks (Frezzotti et al., 2011). In the serpentinites of the Swiss portion of the ZSZ, the peak conditions are estimated at 2.0–2.5 GPa and 600–650 °C (Li et al., 2004b), and in the Italian portion, they are estimated at 2.2–2.8 GPa and 580–620 °C (Rebay et al., 2012). Based on the P–T evolution inferred from the surrounding metabasites, the P–T-peak conditions proposed for rodingites in the Swiss portion of ZSZ (Zermatt area) (Li et al., 2008) are 2.5–2.8 GPa and 600–625 °C (Bucher et al., 2005).

The above-mentioned peak conditions, frequently estimated in the same localities with different methods (pseudosections, classical thermobarometry, phase equilibria), led to the reconstruction, in different portions of ZSZ, of P–T trajectories indicating a heterogeneous metamorphic evolution of this complex. However, in contrast, based on the assemblages from metabasites and calcschists, a homogeneous evolution for the entire ZSZ has been suggested characterized by P–T peak conditions of 2.3 ± 0.1 GPa and 540 ± °C (Angiboust et al., 2009; Angiboust & Agard, 2010). Recently, part of the Monviso ophiolite has been interpreted as forming a single unit with the ZSZ, that would consist of a continuous slab recording a coherent metamorphic evolution (Angiboust et al., 2012). In contrast with the last interpretation, the age data indicate a wide time interval of re-equilibration during subduction of the ZSZ rocks and associated continental slivers between 80 and 40 Ma (with ages interpreted as referred to peak conditions comprised between 58 and 38 Ma; Skora et al., 2009, 2015; Springer et al., 2009; Weber et al., 2015 and references therein) consistent with indications of a heterogeneous metamorphic evolution.

Since the 1960s, rodingites within the Western Alps have been interpreted as former gabbro dykes (Dal Piaz, 1965, 1967, 1969; Bortolami & Dal Piaz, 1968). More recently, different types of rodingites in the ZSZ, that are primarily distinguishable in terms of their mineral content, have been ascribed to different protoliths or degrees of oceanic metasomatic transformation (Li et al., 2004a; Panseri et al., 2008; Zanoni et al., 2012). In the upper Valtournanche, rodingites are considered to have recrystallized during the polyphasic Alpine ductile deformation that affected the hosting serpentinites. Igneous clinopyroxene porphyroclasts are considered the only relicts of gabbro protoliths (Dal Piaz et al., 1980; Li et al., 2004a; Zanoni et al., 2012). In the Lanzo Massif gabbro dykes were rodingitized through interactions with Cretaceous seawater (Rösli et al., 1991) and late Alpine fluids (Castelli et al., 1995), as described in Bellecombe rodingites where HP assemblages are overprinted during greenschist Alpine rodingitization (Ferrando et al., 2010).

Recently, metasomatism during Alpine subduction has been postulated as the source of the main mineral assemblages of rodingites from the ZSZ, and this hypothesis is based on the consistency between thermodynamic modelling and P–T evolution constrained in the metabasites (Li et al., 2008). However, a multiscale continuous structural correlation between rodingite boudins and their country serpentinites indicates that these mineral assemblages were established through HP/UHP re-crystallization of rodingites that developed during Jurassic ocean spreading (Zanoni et al., 2012).

## MESOSTRUCTURES

The mapped area primarily consists of serpentinites and metagabbros, and widespread rodingite boudins enclosed in serpentinites (Fig. 1c). Four ductile deformation stages (D1, D2, D3 and D4) affected the serpentinites, metagabbros and rodingites (Fig. 2). The first three stages are associated with penetrative foliations, whereas the last stage locally produced a new cleavage (Rebay et al., 2012; Zanoni et al., 2012). Serpentinites are normally foliated rocks, but they are massive locally. The metagabbros contain flaser-type structures and in places, preserve igneous textures. The minor calcschists and prasinites that outcrop in the western part of the area (Fig. 1c) usually form metre-thick layers.

In detail, pre-D1 structures cannot be clearly detected at outcrop scale but are well developed at the microscale (see next section). D1 is characterized by a generally steep S1 continuous foliation that primarily dips SSW and NNE and locally is the dominant foliation. The second deformation stage (D2) produces up to metre-sized folds and an S2 axial plane foliation that usually gently dips westward. The D2 folds are characterized by a shallowly plunging A2 axes that primarily trend NNW–SSE and a shallow dipping AP2 axial planes that primarily dip westward. In the serpentinites, the D2 folding produces a shallowly dipping L2 crenulation lineation that primarily trends NNW–SSE. Usually, the S2 foliation (or the composite S1/S2 foliation) is the most pervasive fabric. Rodingite boudins and dykes are generally re-oriented close to the S2 and S1/S2 foliations in the country serpentinites (Figs 2, 3 & 4a). The D3 structures consist of open to tight metre-sized folds and an S3 axial plane foliation, which is a disjunctive cleavage locally and dips WSW at ~60°. The A3 fold axis and the associated L3 crenulation lineation shallowly trend N–S. The D4 stage is responsible for an upright open folding and a rare S4 disjunctive cleavage, which is primarily recorded in serpentinites. Generally, the S4 foliation and AP4 axial plane are sub-vertical and

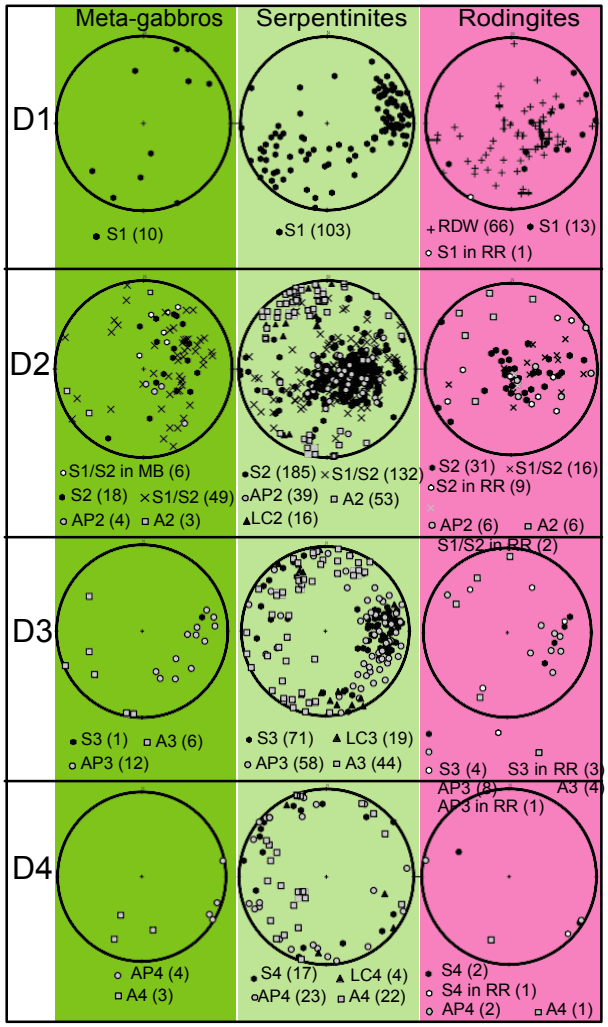


Fig. 2. Synoptic projection of the D1, D2, D3 and D4 structure orientations in serpentinites, metagabbros, and rodingites. S = foliation; A = fold axis; AP = fold axial plane; LC = crenulation lineation; RDW = rodingite dyke wall; RR = reaction rim of rodingites; MB = metabasics associated with the metagabbros. Brackets contain the number of orientation data that are plotted on equal area lower hemisphere projection of planar (pole to plane plot) and linear structures. Please note that the rodingite dyke wall is plotted with D1 structures only for convenience and it can be re-structured during D2 or earlier than D1.

trend NE–SW and the A4 fold axis and L4 crenulation lineation are shallow and trend NE–SW (Fig. 2). Locally, the A4 fold axis and L4 crenulation lineation trend NW–SE, and the AP4 axial planes trend NW–SE, suggesting that D4 folding may involve two conjugate systems or represent two separate groups of structures of an undetectable relative chronology.

In the studied area, extensive outcrops allow for the continuous structural correlation and mapping of the subsequent structures developed during the polyphasic deformation history. The grid of successive foliation trajectories intersecting the boundaries between the different rock types is the basis for this type of correlation, and it is synthesized in the interpretative structural map of Fig. 1c from an original structural mapping at 1:5000 scale.

The entire polyphasic deformation history is recorded in serpentinites and rodingites. Foliations that developed both under eclogite and epidote–amphibolite facies conditions in serpentinites (Rebay et al., 2012) propagate from serpentinites to rodingites (see also Zanoni et al., 2012). The rodingites frequently preserve gabbro-type textures and have 1 cm clinopyroxene porphyroclasts. The structural sketches in Fig. 3 show three outcrop details illustrating the structural correlation between serpentinites and rodingites (visible on the hectometre and decimetre scales in the serpentinites, Figs 3 & 4a) that are used to distinguish the HP/UHP mineral assemblages in rodingites. Locally, single rodingite boudins show compositional and structural heterogeneities (Figs 3 & 4b,c). D3 can produce an intense folding of rodingite boudins, and the S3 crenulation foliation propagates from serpentinites to either rodingites or its reaction rim towards serpentinites (Fig. 4d). This rim, between rodingites and serpentinites, generally consists of chlorite and clinopyroxene schists. The D4 stage is sporadically responsible for the gentle folding of rodingite boudins.

In serpentinites, minerals marking the D2 fabrics developed during the Alpine subduction under eclogite facies conditions at 2.2–2.8 GPa and 580–620 °C, whereas minerals marking the D3 structures formed under epidote–amphibolite facies conditions at 0.7–1.0 GPa and 540–570 °C (Rebay et al., 2012). These P–T estimates have been integrated with the results of the structural correlation, and they represent the framework that will allow benchmarking the conditions under which the mineral assemblages formed in the rodingites, which will be independently tested through petrological modelling.

## MICROSTRUCTURES

Epidote, garnet, Mg-chlorite, clinopyroxene and vesuvianite are the main rodingite-forming minerals. Three rodingite types are defined according to the relative amount and occurrence of these minerals: epidote-bearing, garnet–chlorite–clinopyroxene-bearing, and vesuvianite-bearing rodingites (see also Zanoni et al., 2012). The modal compositions are variable within these three rodingite types, and intermediate modal compositions occur between them. In Fig. 5, the microstructural features of the three types of rodingite are represented. In the following text and figures, the mineral abbreviations are based on Whitney & Evans (2010); the subscripts indicate different generations of each mineral related to Alpine growth and re-crystallization, and the pre-D1 mineral relicts are labelled with the subscript 0.

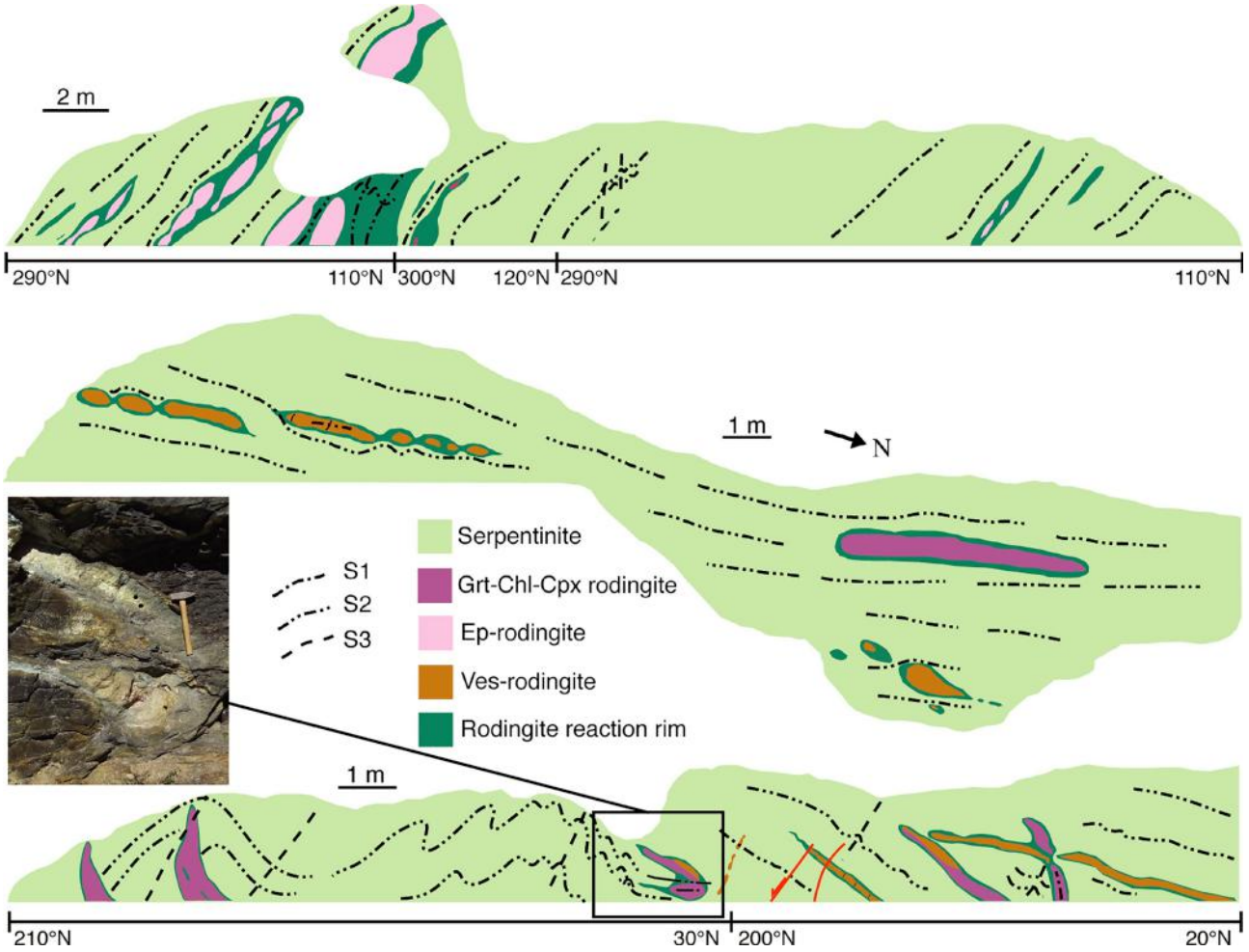


Fig. 3. Structural sketch maps of ~25 to 40 m long continuous outcrops, showing that the same structural history is shared by the serpentinites and hosted rodingites. Relative chronology of superposed foliations is shown in the legend. Photograph illustrates the relationships between garnet–clinopyroxene–chlorite-bearing and vesuvianite-bearing rodingites.

Epidote-bearing rodingites

This type primarily consists of epidote (20–60%), clinopyroxene (15–50%), Mg-chlorite (10–20%), and garnet (≤30%). Titanite, rutile, tremolite and opaque minerals are <5%. S1 is primarily marked by both the SPO (shape preferred orientation) and the LPO (lattice preferred orientation) of epidote$_I$, Mg-chlorite$_I$ and clinopyroxene$_I$, with clinopyroxene$_I$ and minor epidote$_I$ forming aggregates parallel to S1 (Fig. 5a,b). Coarse-grained epidote$_I$ crystals are zoned and enclose garnet$_I$ grains with rational crystal faces (Vernon, 2004). Mg-chlorite$_I$ forms porphyroclasts within S2, which is defined by the SPO and/or the LPO of clinopyroxene$_{II}$, Mg-chlorite$_{II}$, epidote$_{II}$ and rare tremolite$_I$. Epidote$_{II}$ also forms polygonal aggregates and is enclosed in Mg-chlorite$_{II}$. Titanite, partially or totally replacing rutile, is in thin trails parallel to S2 and rarely occurs in the clinopyroxene$_{II}$ layers. S1 and S2 are defined by SPO of up to 1 cm large kinked clinopyroxene$_0$ porphyroclasts (Fig. 5c) that were overgrown by clinopyroxene$_{I/II}$ rims and clinopyroxene$_{I/II}$ spikes parallel to S1 and S2. Locally, opaque minerals grew along clinopyroxene$_0$ cleavages. Epidote$_0$ is both enclosed in clinopyroxene$_0$ porphyroclasts and forms aggregates wrapped by S1 (Fig. 5a). Where S2 is well developed, epidote$_{II}$, clinopyroxene$_{II}$ and garnet$_{II}$ form fine-grained crystals in trails parallel to S2. Clinopyroxene$_0$ porphyroclasts show fractures at a high angle with S2 filled by garnet$_{II}$, clinopyroxene$_{II}$ and rare tremolite$_I$, with SPO parallel to S2, suggesting that they developed during D2. Epidote$_{III}$ fills post-D2 fractures and consists of zoisite or clinozoisite in fractures intersecting epidote$_I$ or epidote$_{II}$ (Fig. 5d) and Fe-epidote in fractures intersecting garnet, clinopyroxene$_{II}$, and Mg-chlorite$_{II}$ aggregates. Rare post-D2 stage tremolite$_{II}$ overgrew garnet and epidote. Rocks containing tremolite have the least epidote. Based on the microstructural features, the

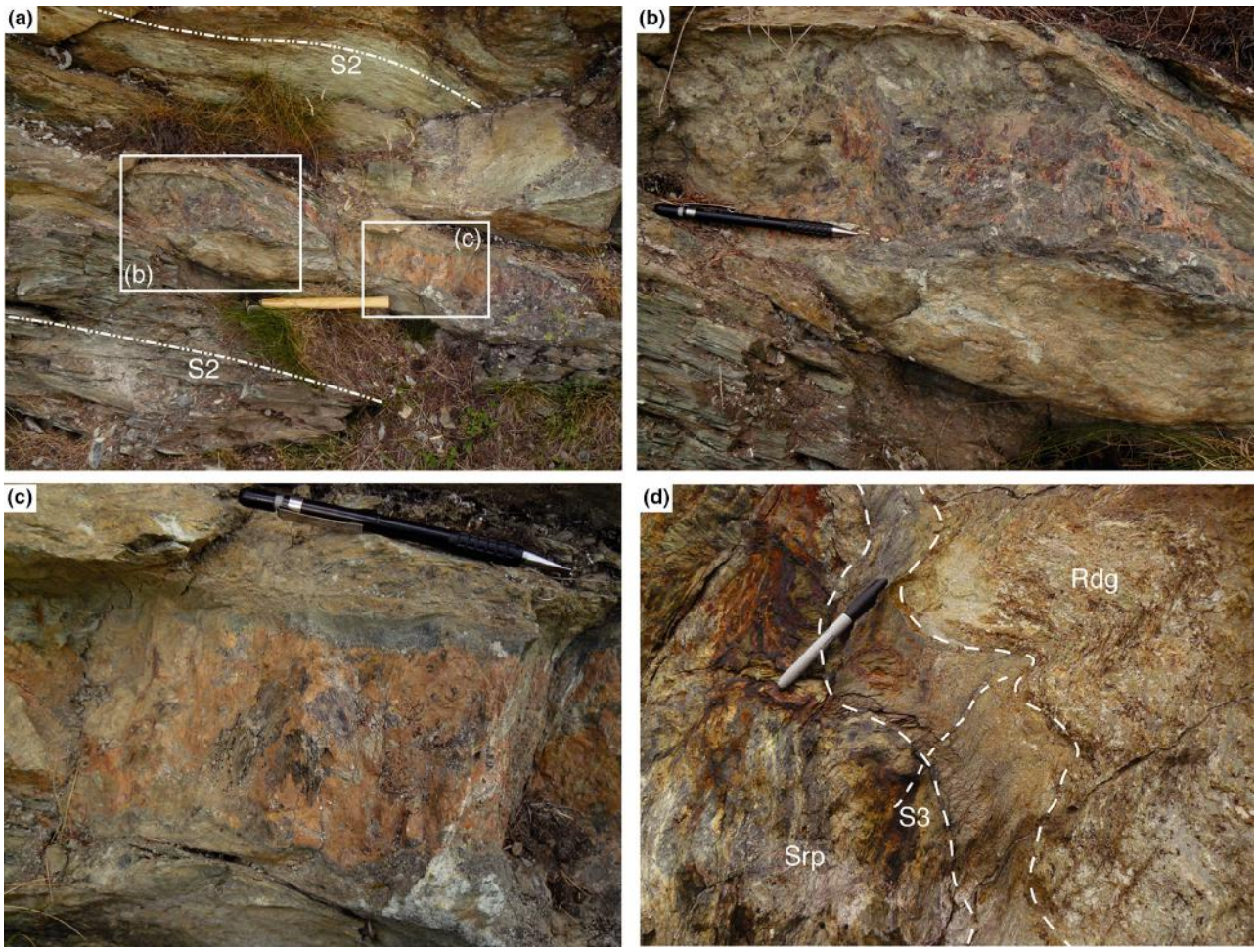


Fig. 4. (a) Rodingite boudin parallel to S2. Hammer for scale. (b) Close up that shows the heterogeneous mineral compositions of the rodingite boudin; the reddish grey area is rich in clinopyroxene porphyroclasts and garnet and the whitish area, close to the top of the picture, is rich in epidote. Pencil for scale. (c) Close up that shows mineral composition and structural heterogeneity in a rodingite boudin; the centre of the boudin has a massif texture affected by a rough foliation, defined by shape preferred orientation of clinopyroxene porphyroclasts, whereas the margin of the boudin records the S2 foliation, which affects serpentinite as well. Pencil for scale. (d) D3 folding associated with S3 foliation refracting from the serpentinite to the sole rodingite reaction rim. Ink marker for scale.

following mineral growth–deformation relationships are inferred in epidote-bearing rodingites (see also Fig. 5a–d):

Pre-D1 mineral relicts: $Cpx_0$ porphyroclasts, $Ep_0$
Syn-D1 assemblage: $Ep_I + Cpx_I + MgChl_I + Grt_I$
Syn-D2 assemblage: $Ep_{II} + Cpx_{II} + MgChl_{II} + Grt_{II} \pm Rt \pm Tr_I$
Post-D2 assemblage: $\pm Ep_{III} \pm Ttn \pm Tr_{II}$.

Garnet–chlorite–clinopyroxene-bearing rodingites

These consist of garnet (20–60%), Mg-chlorite (20–55%), clinopyroxene (≤50%), vesuvianite (≤10%) and opaque minerals (≤5%). These rocks record either S1 or S2 foliations or S2 crenulation cleavage as dominant fabrics (Fig. 5e–g). $Garnet_I$ trails, Mg-$chlorite_I$, $clinopyroxene_I$ (Fig. 5f) and rare $vesuvianite_I$ define the S1 foliation and $garnet_{II}$, Mg-$chlorite_{II}$, $clinopyroxene_{II}$ and ilmenite define the S2 foliation (Fig. 5e–h). Where S1 is pervasive, up to 1 cm large $clinopyroxene_0$ porphyroclasts show fractures filled by fine-grained $garnet_I$ and/or $clinopyroxene_I$, with minor $epidote_I$ and Mg-$chlorite_I$. $Garnet_I$ also rims $clinopyroxene_0$ porphyroclasts. Finally aggregates of $garnet_I$ and minor $clinopyroxene_I \pm$ Mg-$chlorite_I$ are locally parallel to S1 foliation and could represent a complete replacement of the $clinopyroxene_0$ porphyroclasts. The S1 foliation is affected by micro-shear zones defined by Mg-$chlorite_{II}$ and rare $vesuvianite_{II}$. Where S2 is pervasive, $clinopyroxene_0$ is crossed by fractures at a low angle to its cleavages, which are filled by $garnet_{II}$. Wider fractures in $clinopyroxene_0$ contain oblique Mg-$chlorite_{II}$ and minor $clinopyroxene_{II}$ crystals. The S2 foliation is generally a

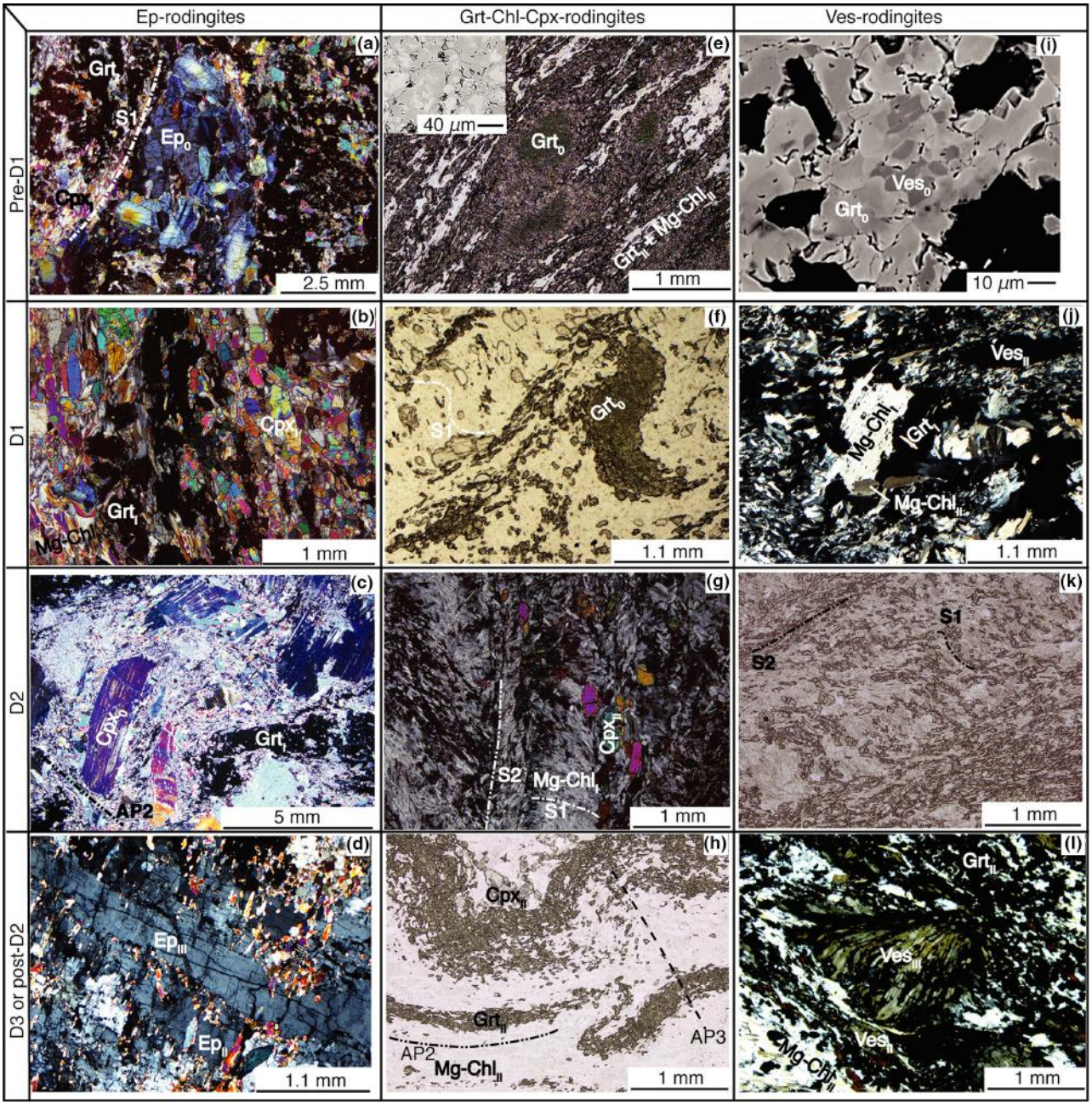


Fig. 5. Relationships between the mineral growth and deformation stages of the three rodingite types that support the reconstruction of equilibrium mineral assemblages and their relative chronology. (a) Relict epidote$_0$ aggregates wrapped by S1 here marked by SPO of clinopyroxene$_I$. Crossed polars. (b) S1 foliation marked by clinopyroxene$_I$, garnet$_I$, epidote$_I$, and chlorite$_I$. Crossed polars. (c) S1, marked by SPO of clinopyroxene$_0$ porphyroclasts, chlorite$_I$ and clinopyroxene$_I$ and garnet$_I$-rich layers, is overprinted by a D2 folding. Clinopyroxene$_I$ also grew in the necks of clinopyroxene$_0$ porphyroclasts. Crossed polars. (d) Epidote$_{III}$-bearing veins intersecting the S2 foliation mostly marked by epidote$_{II}$ and clinopyroxene$_{II}$. Crossed polars. (e) Uvarovitic garnet$_0$ aggregates wrapped by the S2 foliation that is marked by Mg-chlorite$_{II}$ and garnet$_{II}$ trails. Plane polarized light. In the inset (BSE image) a complex zoning pattern of the garnet$_0$ grains. The lighter grey zones are the most Cr-rich. (f) Crenulated S1 cut by S2 films. A relict garnet$_0$ aggregate is preserved between S1 films and folded by D2. Clinopyroxene, garnet, and chlorite mark both foliations. Plane polarized light. (g) S2 crenulation foliation and relict S1. Both foliations are marked by chlorite, clinopyroxene and garnet. Crossed polars. (h) D3 micro-folds overprinting S2 marked by layering of garnet$_{II}$ and chlorite$_{II}$ with minor clinopyroxene$_{II}$. A D2 micro-fold is also preserved. Plane polarized light. (i) Relict vesuvianite$_0$ (darker grey) preserved in garnet$_0$ (lighter grey). BSE image. (j) Mg-chlorite$_I$ and garnet$_I$ marking the relict S1 preserved between vesuvianite$_{II}$ and Mg-chlorite$_{II}$ films. Crossed polars. (k) Crenulated S1 preserved between S2 films; both foliations are marked by vesuvianite, chlorite, and garnet. Plane polarized light. (l) vesuvianite$_{III}$ overprinting S2 foliation marked by vesuvianite$_{II}$, chlorite$_{II}$ and garnet$_{II}$. Crossed polars.

continuous foliation (Fig. 5e); however, where it is incipient it consists of a spaced crenulation cleavage with folded S1 relicts within the S2 films (Fig. 5f). Opaque minerals define an internal foliation in the clinopyroxene$_{II}$ grains that is slightly folded and continuous with the external S2 foliation, thus suggesting clinopyroxene$_{II}$ growth as syn-D2. In the D2 microfolds, Mg-chlorite$_I$ shows internal deformation and Mg-chlorite$_{II}$ forms recrystallized decussate grains. Moreover, locally, garnet$_{II}$ replaces rims and cleavages of pre-D2 Mg-chlorite porphyroclasts. The S1 and S2 foliations wrap green-pleochroic uvarovite-rich garnet$_0$ fine-grained aggregates with a colourless rim accounting for the recrystallization of Cr-rich garnet$_0$ during D1 or D2 (Fig. 5e,f). These aggregates contain Cr-spinel that could be exsolved during garnet recrystallization or may represent relict inclusions in the Cr-rich garnet$_0$. Mg-chlorite$_{III}$ marks the incipient S3 crenulation cleavage of locally asymmetric micro-folds (Fig. 5h). The microstructures indicate the following mineral growth-deformation sequence:

Pre-D1 minerals: Cr-rich Grt$_0$ and Cpx$_0$ porphyroclasts, Cr-rich Spl$_0$ and Mg-Chl$_0$
Syn-D1 or pre-D2 assemblage: Mg-Chl$_I$ + Grt$_I$ ± Cpx$_I$ ± Ep$_I$ ± Ves$_I$ ± Ilm
Syn-D2 or post-D1 assemblage: Mg-Chl$_{II}$ + Grt$_{II}$ + Cpx$_{II}$ ± Ves$_{II}$ ± Ilm
Syn-D3 assemblage: Mg-Chl$_{III}$.

### Vesuvianite-bearing rodingites

These consist of vesuvianite (25–55%), Mg-chlorite (10–55%), garnet (10–30%), clinopyroxene (5–20%) and opaque minerals (≤1%) with uvarovite-rich garnet$_0$ micro-aggregates. These aggregates are wrapped by the S2 foliation, and form a microstructure similar to that described for the garnet–chlorite–clinopyroxene-bearing rodingites, but in contrast, contain euhedral to subhedral vesuvianite$_0$ crystals (Fig. 5i). Layers with different grain size and modal amounts of vesuvianite$_{II}$, clinopyroxene$_{II}$, or garnet$_{II}$ with rare rutile (rimmed by titanite) films and minor epidote define the dominant S2 foliation (Fig. 5j,k). Vesuvianite$_{II}$, clinopyroxene$_{II}$ and Mg-chlorite$_{II}$ have an SPO parallel to S2, and Mg-chlorite$_{II}$ also shows LPO (Fig. 5k). Garnet$_I$ trails, Mg-chlorite$_I$ and vesuvianite$_I$ define relicts (Fig. 5j) or folded surfaces (Fig. 5k) of S1 foliation that is locally preserved within the S2 lithons. S2 wraps 1 mm clinopyroxene$_0$ porphyroclasts that may show an SPO parallel to S2. Minor epidote may grow at the rims of the clinopyroxene$_0$ porphyroclasts. Fine-grained opaque minerals occur within the clinopyroxene$_0$ porphyroclasts but not within their clinopyroxene$_{II}$ rims. This finding suggests that opaque inclusions are exsolved by clinopyroxene$_0$ during Alpine re-equilibration. Vesuvianite$_{II}$ and Mg-chlorite$_{II}$ occupy strain shadows and generally show an SPO parallel to S2 (Fig. 5j,k). In the clinopyroxene$_0$ porphyroclasts, clinopyroxene$_{II}$-bearing fractures cut fractures filled with garnet$_{II}$, Mg-chlorite$_{II}$ and vesuvianite$_{II}$. Both types of fractures are at a high angle with S2 and are interpreted as syn-D2 stage; in this view, the garnet$_{II}$-bearing fractures formed during earlier stages of D2 than clinopyroxene$_{II}$-bearing fractures. The S2 foliation is overgrown by vesuvianite$_{III}$ garbens (Passchier & Trouw, 2005; Fig. 5l) and intersected by Mg-chlorite$_{III}$-bearing veins. Rare Mg-chlorite$_{III}$ also marks an incipient S3 axial plane foliation or intersects S2 at a low angle. The inferred mineral growth–deformation relationships are as follows:

Pre-D1 or pre-D2 minerals: Cpx$_0$, Grt$_0$, Ves$_0$
Syn-D1 assemblage: Mg-Chl$_I$ ± Grt$_I$ ± Ves$_I$
Syn-D2 assemblage: Ves$_{II}$ + Mg-Chl$_{II}$ + Cpx$_{II}$ + Grt$_{II}$ ± Rt ± Ep
Syn-D3 minerals: Mg-Chl$_{III}$ + Ves$_{III}$ ± Ttn.

## MINERAL CHEMISTRY

The mineral compositions from the different assemblages in rodingites were obtained with a Jeol LXA-8200 electron microprobe (WDS; accelerating voltage, 15 kV; beam current, 15 nA) operating at the Dipartimento di Scienze della Terra "A. Desio" of Milano University. Natural silicates were used as standards, and the results were corrected with a conventional ZAF procedure. Proportional formulae were calculated based on the following number of oxygen atoms: 6 pyroxene, 12 garnet, 12.5 epidote, 28 chlorite and 76 vesuvianite. $Fe^{3+}$ was recalculated for garnet, epidote and clinopyroxene based on charge balance. Hereafter, variations in the chemical compositions of successive mineral generations in the different rodingite types are summarized according to the main differences and significant characteristics. Details are given in Tables 1–3 in which the compositional variations refer to different generations in each rodingite type.

### Epidote

In epidote-bearing rodingites, epidote$_{II}$ is zoned from core to rim, where $Fe^{3+}$ decreases and then increases, with an opposite trend in Al (Table 1).

### Clinopyroxene

Generally, clinopyroxene shows a diopsidic composition with the pre-D1 core of 1 cm porphyroclasts richer in the augitic component (Morimoto, 1988) relative to that of the syn-D1 and syn-D2 rims and matrix foliation grains. The clinopyroxene$_0$ porphyroclasts from vesuvianite-bearing rodingites show the lowest augitic content and those from epidote-bearing

Table 1. Selection of mineral compositions in the three rodingite types. Mineral formulae are calculated on the basis of 12.5, 6, and 12 oxygen atoms for epidote, clinopyroxene and garnet respectively. $Fe^{3+}$ was recalculated based on the charge balance. Rdg = rodingite.

| | Epidote | | | Clinopyroxene | | | | | | | Garnet | | | | | |
|---|---|---|---|---|---|---|---|---|---|---|---|---|---|---|---|---|
| | Ep–Rdg | | | Ep–Rdg | | Grt–Chl–Cpx–Rdg | | | Ves–Rdg | | Ep–Rdg | Grt–Chl–Cpx–Rdg | | | Ves–Rdg | |
| | Core – syn-D2 – rim | | | Pre-D1 | Syn-D2 | Pre-D1 | Syn-D1 | Syn-D2 | Pre-D1 | Syn-D2 | Syn-D2 | Pre-D1 | Syn-D1 | Syn-D2 | Pre-D1 | Syn-D2 |
| $SiO_2$ | 38.33 | 38.36 | 38.54 | 52.22 | 54.80 | 52.64 | 55.96 | 55.70 | 54.82 | 55.33 | 38.57 | 37.05 | 37.41 | 37.65 | 36.91 | 39.10 |
| $Al_2O_3$ | 25.33 | 26.91 | 26.37 | 3.09 | 0.65 | 2.48 | 0.04 | 0.08 | 0.11 | 0.09 | 20.63 | 5.97 | 6.55 | 8.87 | 4.13 | 16.51 |
| $TiO_2$ | 0.09 | 0.08 | 0.15 | 0.56 | 0.02 | 0.57 | 0.00 | 0.05 | 0.02 | 0.03 | 0.25 | 0.03 | 0.05 | 0.16 | 0.04 | 0.44 |
| $Cr_2O_3$ | 0.00 | 0.00 | 0.01 | 0.13 | 0.00 | 0.03 | 0.02 | 0.02 | 0.02 | 0.03 | 0.05 | 14.22 | 0.21 | 0.51 | 20.54 | 0.00 |
| $FeO_{tot}$ | 10.29 | 8.37 | 8.83 | 5.49 | 1.63 | 5.18 | 0.44 | 0.69 | 5.01 | 1.16 | 15.47 | 7.43 | 20.21 | 16.73 | 3.88 | 8.51 |
| MgO | 0.08 | 0.08 | 0.07 | 16.01 | 17.01 | 15.15 | 18.08 | 17.91 | 15.08 | 17.55 | 2.17 | 0.03 | 0.02 | 0.14 | 0.07 | 0.38 |
| NiO | 0.03 | 0.04 | 0.03 | 0.05 | 0.05 | 0.03 | 0.03 | 0.03 | 0.02 | 0.02 | 0.00 | 0.00 | 0.00 | 0.00 | 0.00 | 0.02 |
| MnO | 0.07 | 0.17 | 0.29 | 0.16 | 0.33 | 0.15 | 0.09 | 0.10 | 0.22 | 0.03 | 1.32 | 0.30 | 0.14 | 0.40 | 0.26 | 0.33 |
| CaO | 23.36 | 23.79 | 23.80 | 21.57 | 24.63 | 22.78 | 25.79 | 25.56 | 25.43 | 25.97 | 21.89 | 34.38 | 34.77 | 34.52 | 34.40 | 34.99 |
| $Na_2O$ | 0.01 | 0.01 | 0.01 | 0.41 | 0.47 | 0.93 | 0.01 | 0.01 | 0.05 | 0.02 | 0.02 | 0.00 | 0.00 | 0.00 | 0.00 | 0.01 |
| $K_2O$ | 0.00 | 0.00 | 0.00 | 0.00 | 0.00 | 0.01 | 0.00 | 0.00 | 0.01 | 0.00 | 0.00 | 0.00 | 0.00 | 0.00 | 0.00 | 0.00 |
| Total | 97.58 | 97.80 | 98.10 | 99.69 | 99.60 | 99.96 | 100.46 | 100.15 | 100.23 | 99.84 | 100.37 | 99.42 | 99.35 | 98.99 | 100.23 | 100.31 |
| Si | 3.00 | 2.98 | 2.99 | 1.92 | 1.99 | 1.93 | 2.01 | 2.01 | 2.01 | 2.01 | 2.97 | 3.00 | 3.00 | 3.01 | 3.00 | 3.00 |
| $Al^{IV}$ | 0.00 | 0.02 | 0.01 | 0.08 | 0.01 | 0.07 | 0.00 | 0.00 | 0.00 | 0.00 | 0.03 | 0.00 | 0.00 | 0.00 | 0.00 | 0.00 |
| $Al^{VI}$ | 2.34 | 2.45 | 2.41 | 0.05 | 0.02 | 0.03 | 0.00 | 0.00 | 0.01 | 0.00 | 1.84 | 0.57 | 0.62 | 0.84 | 0.39 | 1.49 |
| Ti | 0.01 | 0.00 | 0.01 | 0.02 | 0.00 | 0.02 | 0.00 | 0.00 | 0.00 | 0.00 | 0.01 | 0.00 | 0.00 | 0.01 | 0.00 | 0.03 |
| Cr | 0.00 | 0.00 | 0.00 | 0.00 | 0.00 | 0.00 | 0.00 | 0.00 | 0.00 | 0.00 | 0.00 | 0.91 | 0.01 | 0.03 | 1.32 | 0.00 |
| $Fe^{3+}$ | 0.66 | 0.54 | 0.57 | 0.03 | 0.02 | 0.08 | 0.00 | 0.00 | 0.00 | 0.00 | 0.14 | 0.50 | 1.36 | 1.12 | 0.26 | 0.49 |
| $Fe^{2+}$ | 0.02 | 0.00 | 0.00 | 0.14 | 0.03 | 0.08 | 0.01 | 0.02 | 0.15 | 0.04 | 0.86 | 0.00 | 0.00 | 0.00 | 0.00 | 0.06 |
| Mg | 0.01 | 0.01 | 0.01 | 0.88 | 0.92 | 0.83 | 0.97 | 0.97 | 0.82 | 0.95 | 0.25 | 0.00 | 0.00 | 0.02 | 0.01 | 0.04 |
| Ni | 0.00 | 0.00 | 0.00 | 0.00 | 0.00 | 0.00 | 0.00 | 0.00 | 0.00 | 0.00 | 0.00 | 0.00 | 0.00 | 0.00 | 0.00 | 0.00 |
| Mn | 0.00 | 0.01 | 0.02 | 0.00 | 0.01 | 0.00 | 0.00 | 0.00 | 0.01 | 0.00 | 0.09 | 0.02 | 0.01 | 0.03 | 0.02 | 0.02 |
| Ca | 1.96 | 1.98 | 1.98 | 0.85 | 0.96 | 0.89 | 0.99 | 0.99 | 1.00 | 1.00 | 1.81 | 2.99 | 2.99 | 2.95 | 2.99 | 2.87 |
| Na | 0.00 | 0.00 | 0.00 | 0.03 | 0.03 | 0.07 | 0.00 | 0.00 | 0.00 | 0.00 | 0.00 | 0.00 | 0.00 | 0.00 | 0.00 | 0.00 |
| K | 0.00 | 0.00 | 0.00 | 0.00 | 0.00 | 0.00 | 0.00 | 0.00 | 0.00 | 0.00 | 0.00 | 0.00 | 0.00 | 0.00 | 0.00 | 0.00 |
| New FeO | 0.14 | 0.00 | 0.00 | 4.67 | 1.11 | 2.72 | 0.44 | 0.69 | 5.01 | 1.16 | 13.29 | 0.00 | 0.00 | 0.00 | 0.00 | 0.92 |
| New $Fe_2O_3$ | 11.11 | 9.30 | 9.81 | 0.91 | 0.58 | 2.73 | 0.00 | 0.00 | 0.00 | 0.00 | 2.42 | 8.26 | 22.46 | 18.59 | 4.32 | 8.44 |
| New total | 98.69 | 98.73 | 99.08 | 99.78 | 99.65 | 100.23 | 100.46 | 100.15 | 100.78 | 99.84 | 100.61 | 100.25 | 101.60 | 100.85 | 100.67 | 101.15 |

Table 2. Selection of mineral compositions in the three rodingite types. Mineral formulae are calculated on the basis of 28 and 76 oxygen atoms for chlorite and vesuvianite respectively. Rdg = rodingite.

| | Chlorite | | | | | | Vesuvianite | | | |
|---|---|---|---|---|---|---|---|---|---|---|
| | Ep–Rdg | Grt–Chl–Cpx–Rdg | | | Ves–Rdg | | Ves–Rdg | | | |
| | Syn-D2 | Syn-D1 | Syn-D2 | Syn-D3 | Syn-D2 | Post-D2 | Pre-D1 | Syn-D1 | Syn-D2 | Post-D2 |
| $SiO_2$ | 30.09 | 31.64 | 29.39 | 30.18 | 31.64 | 31.18 | 37.34 | 37.52 | 37.53 | 37.30 |
| $Al_2O_3$ | 20.97 | 19.56 | 19.99 | 18.77 | 19.70 | 20.11 | 17.30 | 17.22 | 16.94 | 19.73 |
| $TiO_2$ | 0.02 | 0.00 | 0.01 | 0.01 | 0.00 | 0.01 | 1.17 | 0.27 | 0.09 | 0.02 |
| $Cr_2O_3$ | 0.01 | 0.03 | 0.00 | 0.12 | 0.06 | 0.14 | 4.13 | 0.01 | 0.04 | 0.04 |
| $FeO_{tot}$ | 5.71 | 1.76 | 12.20 | 12.20 | 1.80 | 1.99 | 1.49 | 2.56 | 3.50 | 1.28 |
| MgO | 29.84 | 32.95 | 25.84 | 25.25 | 32.71 | 32.07 | 0.03 | 2.48 | 2.65 | 1.73 |
| NiO | 0.13 | 0.15 | 0.12 | 0.16 | 0.19 | 0.16 | 0.01 | 0.04 | 0.00 | 0.00 |
| MnO | 0.20 | 0.19 | 0.09 | 0.06 | 0.14 | 0.15 | 0.08 | 0.16 | 0.21 | 0.53 |
| CaO | 0.03 | 0.06 | 0.03 | 0.06 | 0.10 | 0.38 | 36.94 | 36.17 | 36.32 | 35.64 |
| $Na_2O$ | 0.00 | 0.00 | 0.00 | 0.00 | 0.02 | 0.04 | 0.01 | 0.01 | 0.00 | 0.02 |
| $K_2O$ | 0.00 | 0.00 | 0.00 | 0.00 | 0.02 | 0.05 | 0.00 | 0.00 | 0.01 | 0.01 |
| Total | 87.00 | 86.34 | 87.67 | 86.81 | 86.38 | 86.28 | 98.50 | 96.44 | 97.29 | 96.30 |
| Si | 5.74 | 5.95 | 5.75 | 5.96 | 5.95 | 5.89 | 18.15 | 18.25 | 18.12 | 18.12 |
| Al | 4.71 | 4.34 | 4.61 | 4.37 | 4.37 | 4.48 | 9.92 | 9.87 | 9.64 | 11.30 |
| Ti | 0.00 | 0.00 | 0.00 | 0.00 | 0.00 | 0.00 | 0.43 | 0.10 | 0.03 | 0.01 |
| Cr | 0.00 | 0.00 | 0.00 | 0.02 | 0.01 | 0.02 | 1.59 | 0.00 | 0.01 | 0.02 |
| $Fe_{tot}$ | 0.91 | 0.28 | 2.00 | 2.02 | 0.28 | 0.31 | 0.61 | 1.04 | 1.41 | 0.52 |
| Mg | 8.48 | 9.24 | 7.54 | 7.43 | 9.17 | 9.03 | 0.02 | 1.80 | 1.91 | 1.25 |
| Ni | 0.02 | 0.02 | 0.02 | 0.03 | 0.03 | 0.02 | 0.00 | 0.02 | 0.00 | 0.00 |
| Mn | 0.03 | 0.03 | 0.02 | 0.01 | 0.02 | 0.02 | 0.03 | 0.07 | 0.08 | 0.22 |
| Ca | 0.01 | 0.01 | 0.01 | 0.01 | 0.02 | 0.08 | 19.24 | 18.85 | 18.79 | 18.55 |
| Na | 0.00 | 0.00 | 0.00 | 0.00 | 0.01 | 0.02 | 0.01 | 0.01 | 0.00 | 0.02 |
| K | 0.00 | 0.00 | 0.00 | 0.00 | 0.01 | 0.01 | 0.00 | 0.00 | 0.01 | 0.00 |

rodingites show the lowest Ca content. The clinopyroxene$_{II}$ from epidote-bearing rodingites has a higher $Fe^{2+}$ content and a lower and more variable Ca content because of the complex zoning. In all three rodingite types, clinopyroxene$_0$ contains up to 0.02 a.p.f.u. of Ti, whereas in clinopyroxene$_I$ and

Table 3. Compositional range of garnet, epidote, clinopyroxene, vesuvianite and chlorite in atoms per formula unit in the different types of rodingite, during different deformation stages. Mineral compositions predicted by THERMOCALC: x(di) = $Fe^{2+}$/($Fe^{2+}$ + Mg); x(g) = $Fe^{2+}$/($Fe^{2+}$ + Mg); z(g) = Ca/(Ca + $Fe^{2+}$ + Mg).

| | Ep–rodingite | | Grt–Chl–Cpx–rodingite | | | | Ves–rodingite | | | |
|---|---|---|---|---|---|---|---|---|---|---|
| | Pre-D1 | Syn-D2 | Pre-D1 | Syn-D1 | Syn-D2 | Post-D2 | Pre-D1 | Syn-D1 | Syn-D2 | Post-D2 |
| Epidote | | | | | | | | | | |
| $Fe^{2+}$ | | 0.00–0.06 | | | | | | | | |
| $Fe^{3+}$ | | 0.11–0.70 | | | | | | | | |
| Mg | | 0.00–0.01 | | | | | | | | |
| Ca | | 1.92–2.00 | | | | | | | | |
| Al | | 2.29–2.87 | | | | | | | | |
| $X_{Mg}$ | | 0.06–1.00 | | | | | | | | |
| Garnet | | | | | | | | | | |
| $Fe^{2+}$ | | 0.86–0.89 | 0.00–0.01 | 0 | 0 | | 0.00–0.01 | | 0.00–0.10 | |
| $Fe^{3+}$ | | 0.13–0.14 | 0.46–1.14 | 1.14–1.36 | 1.12–1.15 | | 0.26–0.81 | | 0.26–1.37 | |
| Mg | | 0.24–0.25 | 0.00–0.01 | 0.00–0.01 | 0.01–0.02 | | 0.00–0.03 | | 0.01–0.04 | |
| Ca | | 1.78–1.81 | 2.95–2.99 | 2.96–2.99 | 2.94–2.95 | | 2.89–2.99 | | 2.80–2.96 | |
| Al | | 1.87–1.88 | 0.45–0.84 | 0.62–0.84 | 0.79–0.84 | | 0.39–1.42 | | 0.54–1.72 | |
| $X_{Mg}$ | | 0.22–0.23 | 0.72–1.00 | 0.88–1.00 | 1 | | 0.65–1.00 | | 0.11–1.00 | |
| x(g) | | 0.30–0.55 | | | 0.60–0.65 | | | | | |
| z(g) | | 0.20–0.50 | | | 0.75–0.92 | | | | | |
| Clinopyroxene | | | | | | | | | | |
| $Fe^{2+}$ | 0.02–0.14 | 0.01–0.05 | 0.02–0.13 | 0.01 | 0.01–0.02 | | 0.01–0.20 | | 0.01–0.06 | |
| $Fe^{3+}$ | 0.03–0.09 | 0.03–0.05 | 0.00–0.09 | 0 | 0 | | 0 | | 0 | |
| Mg | 0.81–0.88 | 0.83–0.92 | 0.77–0.97 | 0.97 | 0.96–0.97 | | 0.75–0.97 | | 0.91–0.96 | |
| Ca | 0.85–0.93 | 0.88–0.97 | 0.88–1.00 | 0.99 | 0.99–1 | | 0.96–1.00 | | 0.99–1.00 | |
| Al | 0.05–0.19 | 0.02–0.12 | 0.00–0.21 | 0 | 0.001–0.004 | | 0.00–0.10 | | 0.00–0.02 | |
| $X_{Mg}$ | 0.87–0.98 | 0.94–0.99 | 0.86–0.98 | 0.99 | 0.98–0.99 | | 0.79–0.99 | | 0.94–0.99 | |
| x(di) | | 0.02–0.06 | | | 0.03–0.06 | | | | | |
| Chlorite | | | | | | | | | | |
| $Fe_{tot}$ | | 0.87–0.91 | | 0.28 | 0.26–2.31 | 1.91–2.02 | | | 0.24–0.60 | 0.31 |
| Mg | | 8.48–8.52 | | 9.24 | 7.26–9.39 | 7.43–7.51 | | | 8.93–9.30 | 9.03 |
| Ca | | 0.01 | | 0.01 | 0.01–0.04 | 0.01–0.04 | | | 0.01–0.05 | 0.08 |
| Al | | 4.71–4.75 | | 4.34 | 3.82–4.82 | 4.37–4.70 | | | 4.16–4.37 | 4.48 |
| $X_{Mg}$ | | 0.90–0.91 | | 0.97 | 0.76–0.97 | 0.78–0.79 | | | 0.94–0.97 | 0.97 |
| Vesuvianite | | | | | | | | | | |
| $Fe_{tot}$ | | | | | | | 0.59–0.62 | 0.69–1.04 | 1.11–1.54 | 0.17–1.55 |
| Mg | | | | | | | 0.02–0.03 | 1.04–1.80 | 1.64–1.97 | 0.87–1.87 |
| Ca | | | | | | | 19.14–19.24 | 18.48–18.85 | 18.64–18.95 | 18.46–18.82 |
| Al | | | | | | | 9.60–10.13 | 9.87–11.31 | 9.25–9.69 | 9.47–11.60 |
| $X_{Mg}$ | | | | | | | 0.03–0.05 | 0.59–0.66 | 0.52–0.63 | 0.39–0.87 |

clinopyroxene$_{II}$ it is below the detection limit. In the garnet–chlorite–clinopyroxene-bearing rodingites, the Ca and Fe + Mg contents are between that of the epidote-bearing and vesuvianite-bearing rodingites (Table 1).

### Garnet

Garnet$_I$ and garnet$_{II}$ primarily consist of andradite and grossular, although the grains from epidote-bearing rodingites contain almandine, spessartine and pyrope. Garnet$_0$ is characterized by uvarovite that is higher in vesuvianite-bearing relative to the garnet–chlorite–clinopyroxene-bearing rodingites. This relict garnet in the vesuvianite-bearing rodingites shows a gradual variation towards the composition of garnet$_I$ and garnet$_{II}$ grains that are aligned within the matrix foliations. In garnet–chlorite–clinopyroxene-bearing rodingites, the garnet that grew along cleavages and fractures of clinopyroxene$_0$ shows a total of weight percentage <100%. This deficiency is <1.5% and is interpreted as the occurrence of $H_2O$ in garnet (i.e. hydrogrossular molecule). This amount of $H_2O$ is lower than 5–12% $H_2O$ content estimated for garnet from rodingites (e.g. Rossman & Aines, 1991).

### Chlorite

Chlorite is primarily a clinochlore (see Hey, 1954), and in vesuvianite-bearing and epidote-bearing rodingites, chlorite shows lower Fe content compared with that in garnet–chlorite–clinopyroxene-bearing rodingites (Tables 2 & 3). Chlorite composition is therefore dependent upon rock bulk chemistry.

### Vesuvianite

Vesuvianite shows a clear compositional variation from the pre-D1 to post-D2 generations. Vesuvianite$_0$ shows higher Cr, Ca and Ti and a lower Mg relative to vesuvianite of later generations. Vesuvianite$_I$ and vesuvianite$_{II}$ are richer in Fe and Mg, whereas vesuvianite$_{III}$ is richer in Al (Table 2; Fig. 6).

## METAMORPHIC EVOLUTION

The assemblages associated with the different recrystallization episodes are very similar and always involve

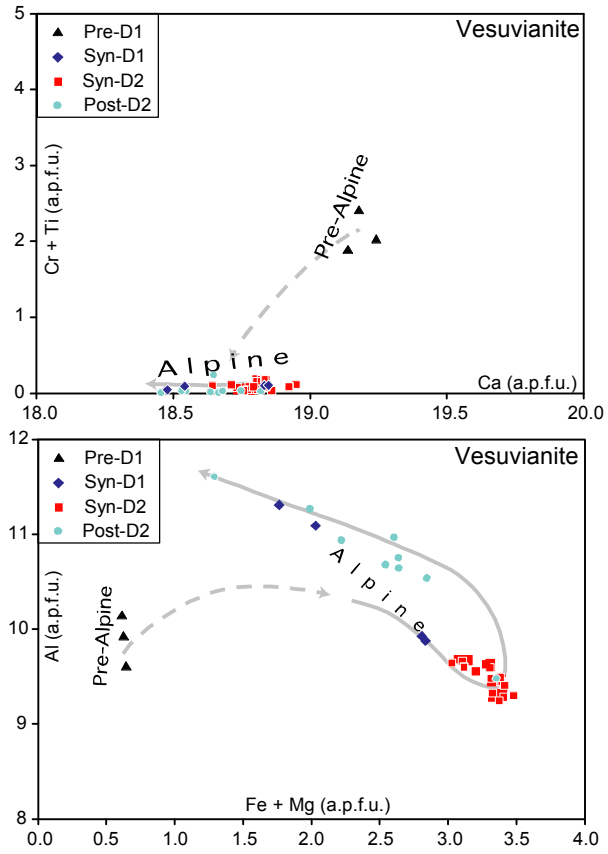


Fig. 6. Variation in the chemical composition of vesuvianite marking successive fabric elements in the vesuvianite-bearing rodingites. Pre-Alpine (pre-D1) vesuvianite displays higher Cr, Ti, and Ca and lower Fe + Mg compared with Alpine (syn-D1, syn-D2 and post-D2) vesuvianite. Higher Fe + Mg values characterize the syn-D2 vesuvianite. Cations are in atoms per formula unit.

clinopyroxene, garnet, chlorite, epidote and vesuvianite, as described above. Nonetheless the mineral compositions vary, as indicated in the mineral chemistry section (Table 3), suggesting that a set of continuous reactions took place. Such reactions imply that the minerals associated with different assemblages change their modal quantities (as shown below) and compositions during successive deformation stages.

In epidote-bearing rodingite the transition from pre-D2 to D2 assemblages derives from reactions such as

$$\text{Cpx} + \text{Ep} + \text{Grt} = \text{Grt} + \text{Cpx} + \text{Mg-Chl} + \text{Ep} + \text{Rt} \pm \text{Tr}$$

and from D2 to D3 such as

$$\text{Grt} + \text{Ep} + \text{Rt} = \text{Mg-Chl} \pm \text{Ttn} \pm \text{Tr}:$$

In garnet–chlorite–clinopyroxene-bearing rodingite a reaction involving spinel would be required to account for observed textures and mineral composition changes from pre-D1 to syn-D1 assemblages:

$$\text{Cpx} + \text{Mg-Chl} + \text{Grt} + \text{Spl} = \text{Cpx} + \text{Mg-Chl} + \text{Grt} + \text{Ilm}:$$

Syn-D1 to syn-D2 mineral assemblage changes can be the result of

$$\text{Cpx} + \text{Grt} + \text{Mg-Chl} \pm \text{Ep} = \text{Cpx} + \text{Mg-Chl} + \text{Grt} + \text{Ilm}:$$

Finally the sporadic occurrence of vesuvianite in the syn-D2 assemblage can be explained by the reaction

$$\text{Mg-Chl} + \text{Grt} + \text{Ep} = \text{Mg-Chl} + \text{Grt} + \text{Ves}:$$

In vesuvianite-bearing rodingites, besides reactions similar to those already described for the other rodingite types, vesuvianite involving reactions occur from pre-D2 parageneses to syn-D2 assemblage and can be summarized by

$$\text{Cpx} + \text{Ves} = \text{Mg-Chl} + \text{Ves}$$

to account for the increase of Fe and Mg and decrease of Al from $\text{vesuvianite}_0$ towards $\text{vesuvianite}_{II}$. A reaction such as

$$\text{Grt} + \text{Ves} = \text{Ves}$$

accounts for the increase in Al and decrease in Fe and Mg from $\text{vesuvianite}_{II}$ to $\text{vesuvianite}_{III}$.

## P–T modelling of the HP/UHP mineral assemblages in rodingite

A P–T grid was calculated in the MASH subsystem, using the end-members of the main silicates observed in the rodingites, that is, garnet, chlorite,

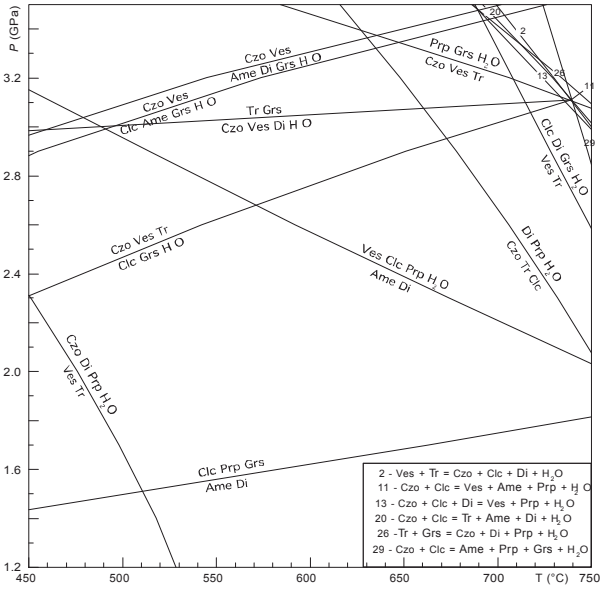


Fig. 7. P–T projection calculated using end-members in the MASH system showing that the main minerals observed in rodingites are stable in the considered P–T window in this subsystem.

clinopyroxene, epidote and vesuvianite (Fig. 7). It is shown that all these minerals are stable over a wide range of P–T conditions, at pressures up to 3.5 GPa and at temperatures below 750 °C, as suggested by the reactions listed above.

Rodingite was modelled in the NCFMASHTO system and phase equilibria were calculated using THERMOCALC (Powell et al., 1998; tc335i upgrade) and the internally consistent thermodynamic data set (Holland & Powell, 1998; tc-ds55, Nov. 2003). The amphibole and pyroxene activity–composition models are those of Diener et al. (2007) and Green et al. (2007) respectively. The garnet models are from White et al. (2007) (however, the garnet asymmetry includes $a_{Grs} = 3$ and $a_{Adr} = 3$ instead of 9), and the Fe–Ti oxide and epidote models are from Holland & Powell (1998). Chlorite is from Holland et al. (1998). The THERMOCALC ax file used is based on that used in Rebay et al. (2010). The other phases are pure end-members: lawsonite, rutile, titanite, quartz, vesuvianite and $H_2O$.

The rock compositions used in the phase equilibria modelling correspond to 'representative mean' rodingite compositions that were estimated through a modal analysis (image analysis based on thin sections and EBS images) of the observed samples and calculated using measured mineral compositions that have been interpreted as contemporaneous to D2. It was also compared to previously published whole-rock

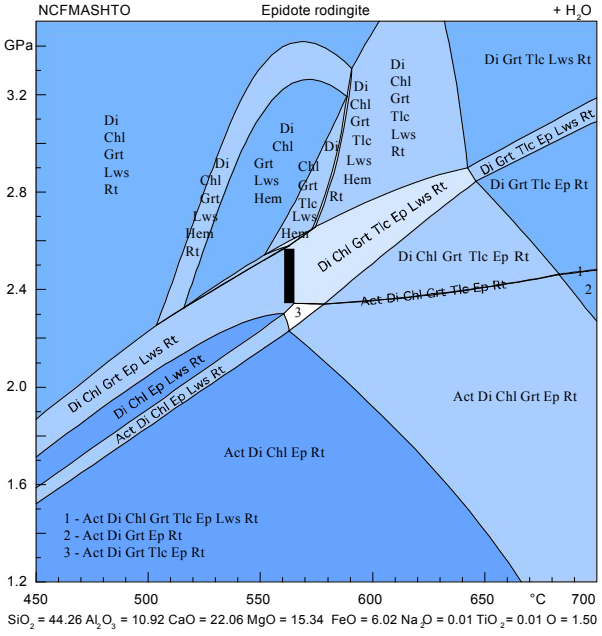


Fig. 8. P–T pseudosection calculated in the NCFMASHTO system with $H_2O$ in excess for a bulk composition that represents epidote-bearing rodingites and is indicated in the figure and expressed in moles. See the detailed comment in the text. The syn-D2 assemblage matches well the stability field of Di, Chl, Grt, Tlc, Ep and Rt, in bold fonts.

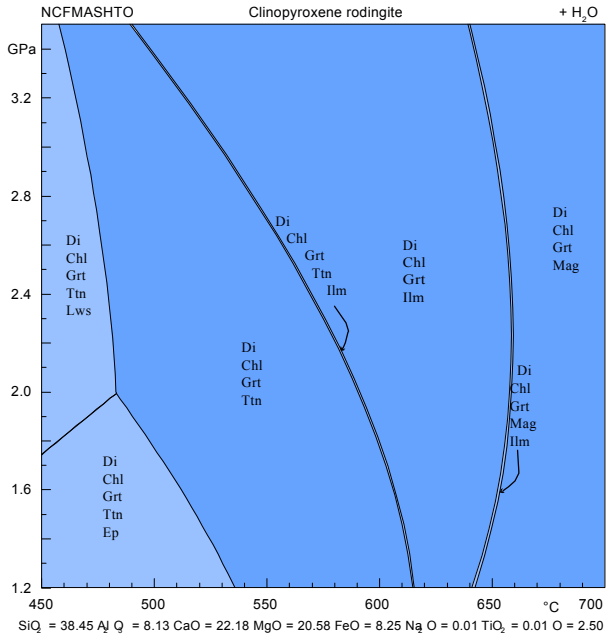


Fig. 9. P–T pseudosection calculated in the NCFMASHTO system with $H_2O$ in excess for a bulk composition that represents garnet–chlorite–clinopyroxene-bearing rodingites and is indicated in the figure and expressed in moles. See the detailed comment in the text. The syn-D2 assemblage matches well the stability field of Di, Chl, Grt and Ilm, in bold fonts.

analyses of rodingites from the ZSZ and China (see Dal Piaz, 1967; Dal Piaz et al., 1980; Li et al., 2007, 2008). The compositions used for the calculation of the pseudosections are indicated in Figs 8 and 9 and expressed in mol.%. Because rodingites are extremely heterogeneous on the outcrop and thin-section scale, due to the efficiency of ocean floor metasomatic processes, a single sample composition was not sufficient for modelling (the rock volumes needed to determine the composition via analytical techniques are always larger than the equilibrium volume needed for modelling); rather, two end-members of the wide range of compositions were selected.

Fixed values of O content (which expresses the O available to produce $Fe^{3+}$-bearing minerals, see Rebay et al., 2010) have been chosen to be 1.5 and 2.5, respectively, as calculated from the modal quantity of $Fe^{3+}$-bearing minerals in the samples, and are likely to represent a minimum possible 'oxidation state' for such samples. Notwithstanding the discussion on fluid in rocks during metamorphism in studies such as Guiraud et al. (2001) and Rebay et al. (2010), the modelling was performed with $H_2O$ occurring in excess because $H_2O$-bearing phases consistently occur in the three analysed rodingite types.

The compositions of syn-D2 minerals (Table 3) were related to the pseudosections, because identifying the peak conditions and determining the stable assemblages at the peak P–T conditions were the objectives. The vesuvianite-bearing rodingites have

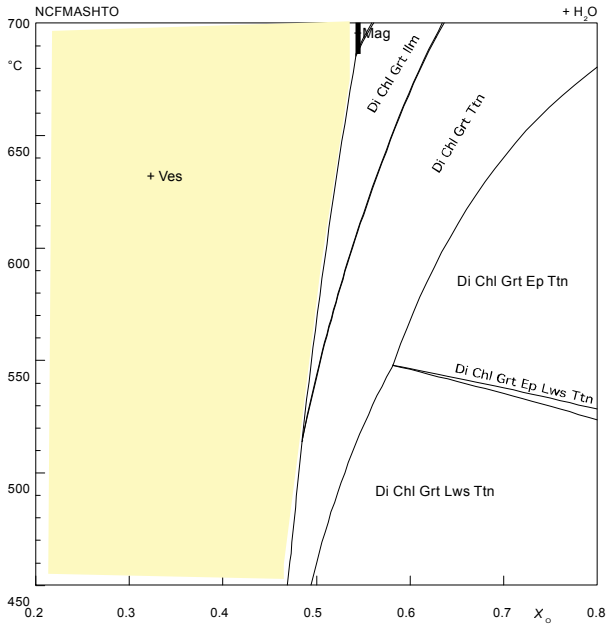


Fig. 10. P–$X_O$ pseudosection calculated in the NCFMASHTO system with $H_2O$ in excess for a bulk composition that represents garnet–chlorite–clinopyroxene rodingites, varying the O content from 0.2 to 0.8, where 0.2 corresponds to 0.97 O and 0.8 to 3.9 O (in moles).

not been modelled, although they constitute a compositional end-member that represents the highest degree of oceanic metasomatism represented in Valtournanche (see Zanoni et al., 2012). This choice is primarily because appropriate a–x models are not available for vesuvianite. Notwithstanding these limitations, we have nonetheless added a T–$X_O$ pseudosection using the composition of garnet–chlorite–clinopyroxene-bearing rodingite and varying the O content from 0.2 to 0.8, where 0.2 corresponds to 0.97 O and 0.8 to 3.9 O (in moles). We have also added the end-member vesuvianite, to show that varying degrees of oxidation state can influence the predicted assemblages and produce the observed ones also in the case of compositions where only the degree of oxidation varies. In Fig. 10 the coloured field towards low O contents, is the one in which the Mg end-member of vesuvianite is predicted to be stable. This is an approximation, as the vesuvianite observed in the rodingites studied is usually rather Fe-rich, the most Mg-rich (with $X_{Mg}$ = 0.6–0.7) being that in the syn-D2 HP assemblage. At higher O contents, the predicted assemblages are those described next.

The general topology of the two pseudosections is quite different. The Al-rich and Si-rich compositions associated with the epidote-bearing rodingite (Fig. 8) result in the presence of epidote together with diopside and garnet, with minor Mg-rich and Al-rich phases such as talc or an increasing amount of amphibole at lower pressures. The P–T space is crossed diagonally by a sequence of fields that separate a region of lower temperature and higher pressure (where lawsonite is stable) from a region of lower pressure and higher temperature (where epidote is stable). The Ti-bearing phase is rutile, which is always present except for a small area between 2.3 and 3.2 GPa and 500–600 °C where hematite is stable. The assemblages observed in the epidote-bearing rodingite are best represented by the field of diopside, chlorite, garnet, talc, epidote and rutile at 2.3–2.8 GPa and 580–680 °C although talc, which is not observed in our rocks, is predicted to occur in small modal quantities of <4%.

The garnet–chlorite–clinopyroxene-bearing rodingite pseudosection of Fig. 9 is characterized by a series of vertical fields involving diopside, chlorite and garnet in different modal amounts, and distinguished by different accessory Fe–Ti-bearing phases: titanite at lower temperatures (<600 °C) ilmenite at intermediate temperatures and magnetite at higher temperatures (>650 °C), at the chosen O content. If different quantities of O are considered, such fields remain stable over a certain composition interval (see Fig. 10). The temperatures are constrained at values <650 °C because magnetite is never observed in the samples; therefore, the temperature range valid for

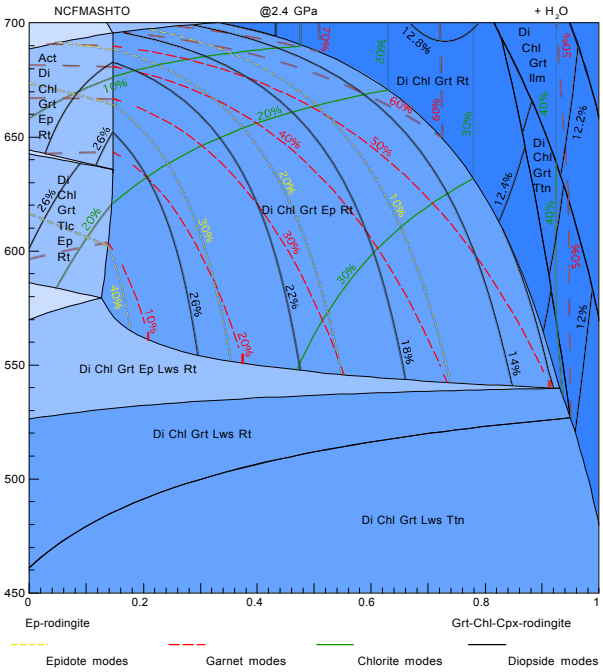


Fig. 11. T–X pseudosection detailing how paragenesis changes with varying temperature at 2.4 GPa pressure. The composition varies between that of epidote-bearing (on the left) and garnet–chlorite–clinopyroxene-bearing rodingites, which represent the intermediate composition of epidote- bearing and vesuvianite-bearing end-members. The field containing the minerals observed in all of the rodingite is contoured for the modal contents of each mineral at changing compositions as explained in the text.

epidote-bearing rodingite is limited. At <500–530 °C, lawsonite is stable ~1.9 GPa and epidote is stable below that pressure and at higher temperatures. A combination of all of the above-described petrological constraints indicates that the P–T-peak conditions for rodingites are 2.3–2.8 GPa and 580–660 °C.

An initial exploration of the effects of variations in the bulk composition of the rodingites was modelled through a T–X pseudosection, where X changes from epidote-bearing to garnet–chlorite–clinopyroxene-bearing rodingite (Fig. 11) calculated at 2.4 GPa. For temperatures <550 °C, lawsonite, which was detected in the Valtournanche metabasite as relicts replaced by paragonite, epidote and minor albite (e.g. Skora et al., 2015), has been never observed in the rodingites, even if it is predicted to be stable at these temperatures. For temperatures >580 °C and up to 680 °C, most of the rodingite compositions are characterized by assemblages involving different modal amounts of diopside, chlorite, garnet, epidote and rutile. The presence of different accessory Fe-Ti-rich phases is addressed in the P–T pseudosections of Figs 8 and 9. As expected, the modal compositions of rodingite, in terms of the four major mineral constituents, is highly dependent on their bulk composition as evidenced by the modal amount of isolines in Fig. 11. The modal amounts of garnet and epidote are primarily dependent on the Ca and Fe–Mg contents of the rocks. The amount of chlorite is also dependent on the temperature because it is consumed towards high temperatures. For a single line connecting epidote-bearing to garnet–chlorite–clinopyroxene-bearing rodingite and along which eight components of the system are contemporaneously changed (considering excess $H_2O$), clinopyroxene presents a maximum of 30% near the epidote-bearing rodingite end-member and then decreases, and it finally increases again towards the garnet–chlorite–clinopyroxene-bearing rodingites. This finding indicates the important effects of bulk composition on the mineral modal amounts. The garnet modal amount is higher at a higher temperature for intermediate compositions (up to 70%), although it decreases with temperature and towards the two compositional end-members. Indeed, rocks that are extremely rich in garnet are described in the rodingite literature. In summary, the modal compositions calculated for the epidote-bearing and garnet–chlorite–clinopyroxene-bearing rodingites, and all of the compositions between these two end-members, account for the modal compositions that are observed in the actual samples and summarized in the microstructural description. Also, the predicted compositions of syn-D2 clinopyroxene and garnet between the two compositional end-members match the measured compositions, within an error less than 2–5%. The model in Fig. 11 indicates that the entire array of observed assemblages may be produced for rodingite under HP/UHP conditions, starting from protoliths rodingitized on the ocean floor without invoking HP metasomatism. Modelling the same compositions without excess $H_2O$ led to the paragenesis predictions that were similar to what was predicted with excess $H_2O$, thus excluding the possibility that the observed parageneses occurred in the presence/absence of fluids under HP conditions. However, the hypothesis of metasomatism occurring also under HP/UHP conditions cannot be completely excluded as suggested by Li et al. (2008).

## DISCUSSION

### Ocean floor record

Uvarovite-rich $garnet_0$ is interpreted as having formed during the oceanic rodingitization of former gabbro dykes (e.g. Mogessie & Rammlamair, 1994; Akizawa et al., 2011). $Vesuvianite_0$ is preserved as inclusions in $garnet_0$ (from vesuvianite-bearing rodingites), and it shows the highest Cr and Ti (Fig. 6), which is distinctive and consistent with its generation during the serpentinization of peridotite (e.g. Kobayashi & Kaneda, 2010), and the full occupancy of the $X + X^0$ site (high content in Ca), which is characteristic of low-grade metamorphism (Gnos & Armbruster, 2006). These features are consistent with $vesuvianite_0$ as resulting from oceanic metasomatism. Because $garnet_0$ and $vesuvianite_0$ occur in the garnet–chlorite–clinopyroxene-bearing and vesuvianite-bearing rodingites, we suggest that the progress of oceanic metasomatism increases from protoliths of HP epidote-bearing to HP vesuvianite-bearing rodingites. This interpretation is also supported by the bulk composition of the three rodingite types, which shows an increase in CaO and MgO and a decrease in $SiO_2$ from epidote-bearing to vesuvianite-bearing rodingites (see also Zanoni et al., 2012 and Fig. 12); these trends are consistent with the metasomatic processes that likely are responsible for rodingite formation at the ocean floor (Schandl et al., 1989; Dubińska et al., 2004). Accordingly, the augitic component in the $clinopyroxene_0$ porphyroclasts decreases from epidote-bearing to vesuvianite-bearing rodingites. All of these data indicate that the three rodingite types are the results of different degrees of oceanic metasomatism; therefore, they represent Tethyan geochemical signatures that were preserved despite the Alpine subduction-related metamorphism and deformation. A similar hypothesis that includes different degrees of oceanic metasomatism in rodingites has been inferred for metaophiolite from the Betic Cordillera that underwent Alpine subduction (Puga et al., 1999). In the Alps, oceanic rodingitization has also been inferred in the Mount Avic massif (Panseri et al., 2008), and additional relicts of oceanic metasomatism that survived the Alpine subduction are represented by Mn-bearing ore deposits at the Praborna mine (Tumiati et al., 2010) and sulphide deposits at the Beth and Servette mines (Giacometti et al., 2014).

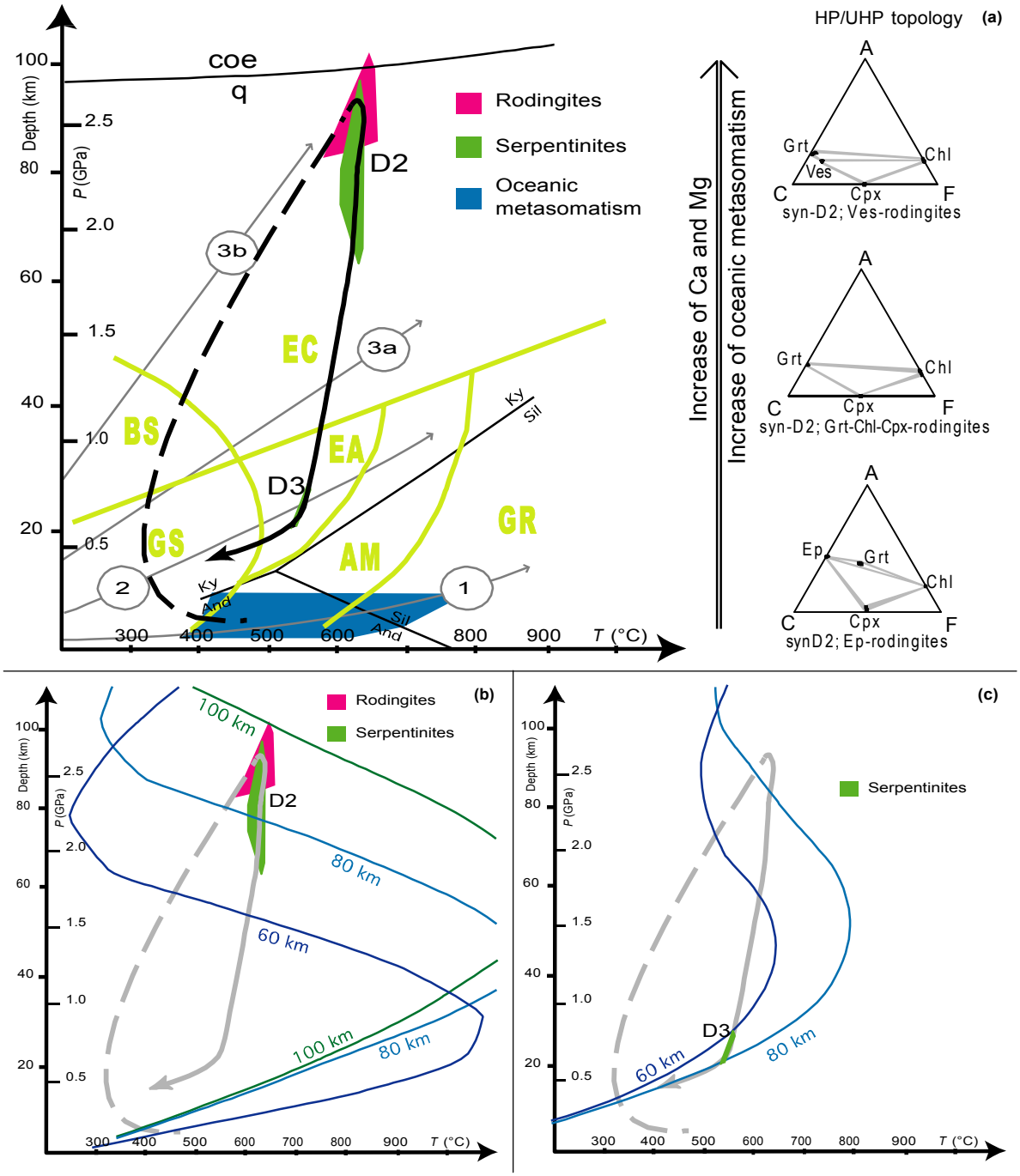


Fig. 12. (a) Peak conditions recorded during the Alpine subduction by the Valtournanche rodingites compared with the conditions recorded in the surrounding serpentinites (after Rebay et al., 2012). ACF diagrams showing the syn-D2 topology in the different rodingite types are modified from Zanoni et al. (2012). Metamorphic facies are after Spear (1993). Geotherms are based on Cloos (1993): (1) near spreading ridge or volcanic arc, (2) normal old plate interior gradient, (3a) 'warm' subduction zones and (3b) cold subduction zones. Conditions for oceanic metasomatism are based on the stability field of vesuvianite according to Ito & Arem (1970), Hoisch (1985), and Valley et al. (1985). The dashed black line indicates the possible P–T path from oceanic metasomatic conditions to the HP/UHP conditions reached during the Alpine subduction and the solid black line indicates the P–T–d–t exhumation path from the HP/UHP conditions to D3 epidote–amphibolite facies conditions that were estimated from the serpentinites (Rebay et al., 2012). (b) Peak conditions recorded by serpentinites and rodingites compared with the geotherm configuration predicted for a subducting system 40 Ma after the onset of the oceanic subduction at 60, 80 and 100 km away from the trench (Spalla & Marotta, 2007). (c) D3 conditions recorded in serpentinites (Rebay et al., 2012) compared with the geotherm configuration predicted for a convergent system c. 8 Ma after the onset of the continental collision at 60 and 80 km away from the trench (Spalla & Marotta, 2007).

## Alpine convergence record

The modelled parageneses expected under HP/UHP for a wide range of rodingite compositions confirm that the observed parageneses and mineral composition are stable at HP/UHP conditions and indicate that the Valtournanche rodingites were mostly re-equilibrated along with the hosting serpentinites during the Alpine subduction at the limit of the coesite stability field. As noted by Rebay et al. (2012), this finding indicates that this portion of the ZSZ experienced pressures that were higher than previously reported, and similar to those registered from the rocks of Cignana (Reinecke, 1991), suggesting that the UHP units are likely larger and/or more abundant than those previously detected. In addition, our work clearly indicates that minerals such as vesuvianite, which has been traditionally considered an indicator of low-P and fluid-rich metamorphic environments, can be stable with peculiar compositions under HP/UHP conditions, provided the presence of a suitable Ca/Si ratio in the bulk composition (≥0.55; Zanoni et al., 2012 and references therein). Microstructures and mineral compositions indicate that vesuvianite evolves through a series of continuous reactions, remaining stable throughout the entire metamorphic evolution once it is formed at the ocean floor. Also, the $H_2O$ in garnet of the ZSZ rodingites, which is lower than that of the typical rodingite garnet (e.g. Rossman & Aines, 1991), may have resulted from the recrystallization under HP/UHP conditions during the Alpine subduction, in agreement with the observed dehydration of serpentinite where syn-D2 Alpine olivine and clinopyroxene are generated (Rebay et al., 2012).

Figure 12a compares the P–T peak with those estimated in the surrounding serpentinites and reports the range of P–T conditions for oceanic evolution. The petrological modelling is supported by the microstructural analysis of both the rodingites and surrounding serpentinites and provide a P–T–d–t path that indicates that these rocks experienced conditions of high pressure approaching the ultrahigh pressure field (2.3–2.8 GPa and 580–660 °C) during the D2 deformation stage; therefore, the rodingites recrystallized in the Alpine subduction system after they were produced by metasomatism under ocean floor-metamorphism conditions. Oceanic evolution is shown by the igneous relicts from gabbro dykes that were subsequently converted into rodingites over the course of the Jurassic evolution of the Alpine Tethys. Successively, the exhumation is marked by an epidote–amphibolite facies re-equilibration that developed in the syn-D3 stage (Rebay et al., 2012) and is characterized by a slight temperature decrease during decompression. The thermal state suggested by the syn-D2 P–T conditions (Fig. 12) is close to that of cold subduction zones (Cloos, 1993), indicating a re-equilibration recorded during active oceanic subduction. In support of this interpretation, a recent model simulating ablative subduction in the Alps predicted similar $P_{Tmax}$ values for the markers of the subducted oceanic lithosphere, which were exhumed by mantle wedge convection prior to the continental collision (Roda et al., 2012). Figure 12b compares the peak conditions estimated for the rodingites and their hosting serpentinites with geotherms computed for an ocean/continent subduction system, converging with a rate of 5 cm $yr^{-1}$ (Spalla & Marotta, 2007). These peak conditions, which are recorded at depth between 102 and 63 km, fit well with geotherms predicted for distances between 70 and 100 km from the trench (Fig. 12b) 40 Ma after the onset of the oceanic subduction. This time interval is coherent with the ages estimated for the peak conditions in ZSZ eclogitized ophiolites.

The D3 deformation stage was accomplished under epidote–amphibolite facies conditions, thus indicating a transition towards a higher thermal state that is compatible with plate interior gradients (Cloos, 1993) and therefore suggests an exhumation that occurred in later stages within a collisional setting (Fig. 12a). Alternatively, similar higher thermal states are predicted to have occurred before the continental collision at the boundary of the supra-subduction convective mantle wedge and towards the upper continental plate, where the subducted oceanic and continental material driven by the rigid buttress of non-hydrated lithospheric mantle can be exhumed (Regorda et al., 2013). To provide further insight into the rate of geodynamic processes during the Alpine convergence, the duration of the subduction–exhumation cycle should be investigated in more detail, to determine the wide span of radiometric ages proposed for the ZSZ metaophiolites (between 80 and 36 Ma; Rubatto et al., 1998; Lapen et al., 2003; Gouzu et al., 2006; Skora et al., 2009; Springer et al., 2009; de Meyer et al., 2014; Weber et al., 2015 and references therein), which are associated with syn-D2 $P_{Tmax}$ estimated conditions. This exhumation can be accomplished during continental collision considering the end of oceanic subduction either at 44 or 40 Ma (Rubatto et al., 1998; Lapen et al., 2003; Gouzu et al., 2006). Indeed Fig. 12c compares the syn-D3 condition estimated in serpentinites (Rebay et al., 2012) with the geotherms computed in a convergent system 8 Ma after the onset of the continental collision (Spalla & Marotta, 2007). The syn-D3 conditions, which are recorded at depth between 20 and 28 km, fit well the geotherms predicted between 60 and 80 km away from the trench. The interplay between the estimated depth and the fitting with geotherms at different distances from the trench for the peak and syn-D3 conditions allows describing the displacement of the ZSZ rocks during their exhumation (Fig. 12b,c). From subduction peak conditions to syn-D3 conditions, the rocks would be displaced vertically of ~60 km and horizontally, towards the

trench, of ~15 km, over a time interval of a few million years at least.

## CONCLUSIONS

The Valtournanche rodingites were studied in the context of the metamorphic evolution already determined for the enclosing serpentinites. It is inferred that rodingite compositions are mostly inherited from metasomatic processes that took place at the Tethys ocean floor and are not modified, other than in mm-scale volumes, in the following Alpine evolution. Thus, the pre-Alpine bulk rock compositions acquired by these former gabbro dykes survived the structural and textural re-equilibration of the rodingite during the Alpine convergence, reflecting different degrees of oceanic metasomatism. The metasomatic minerals, among which vesuvianite, recrystallized in a series of continuous reactions, changing their composition while remaining stable even to HP/UHP conditions estimated to be 2.3–2.8 GPa and 580–660 °C for syn-D2 assemblages. The metamorphic evolution recorded in the rodingites is consistent with syn-D2 deformation taking place under a cold subduction environment and syn-D3 exhumation under a geothermal state compatible with a continental collision. Both syn-D2 and syn-D3 deformation stages took place during the Alpine convergence at minimal ages of c. 40 Ma and 35 Ma respectively. Finally, our results open the debate over the dimension and distribution of HP/UHP units in the Alps, pointing out that possibly the UHP units are more widespread and larger than that thought earlier.

## ACKNOWLEDGEMENTS

K. Bucher and an anonymous reviewer provided insightful and constructive advice that improved the clearness of the paper together with D. Robinson precious suggestions. We thank R. Powell for providing critical discussion, J. Bernardoni for field and laboratory work during his M.Sc. thesis, C. Malinverno for preparing thin sections and A. Risplendente for assisting the microprobe work. G.R. performed the petrological modelling. This work was supported by PRIN 2010-2011: 'Birth and death of oceanic basins: geodynamic processes from rifting to continental collision in Mediterranean and circum-Mediterranean orogens'. D.Z. acknowledges funding from the project: 'Deformazione e metamorfismo delle ofioliti di alta pressione nelle Alpi Occidentali', Università di Pavia.

## REFERENCES

Akizawa, N., Arai, S., Tamura, A. & Uesugi, J., 2011. Chromite and uvarovite in rodingite from the lowermost crust of Oman ophiolite: Cr mobility in hydrothermal condition. Japan Geoscience Union, Makuhari, Chiba, Japan, SCG067-01.

Angiboust, S. & Agard, P., 2010. Initial water budget: the key to detaching large volumes of eclogitized oceanic crust along the subduction channel? Lithos, 120, 453–474.

Angiboust, S., Agard, P., Jolivet, L. & Beyssac, O., 2009. The Zermatt-Saas ophiolite: the largest (60-km wide) and deepest (c. 70–80 km) continuous slice of oceanic lithosphere detached from a subduction zone? Terra Nova, 21, 171–180.

Angiboust, S., Langdon, R., Agard, P., Waters, D. & Chopin, C., 2012. Eclogitization of the Monviso ophiolite (W. Alps) and implications on subduction dynamics. Journal of Metamorphic Geology, 30, 37–61.

Austrheim, H. & Prestvik, T., 2008. Rodingitization and hydration of the oceanic lithosphere as developed in the Leka ophiolite, north–central Norway. Lithos, 104, 177–198.

Bach, W. & Klein, F., 2009. The petrology of seafloor rodingites: insights from geochemical reaction path modeling. Lithos, 112, 103–117.

Ballèvre, M. & Merle, O., 1993. The Combin fault: compressional reactivation of a Late Cretaceous – Early Tertiary detachment fault in the Western Alps. Schweizerische Mineralogische Petrographische Mitteilungen, 73, 205–228.

Barnicoat, A.C. & Fry, N., 1986. High-pressure metamorphism of the Zermatt-Sass ophiolite, Switzerland. Journal of Geological Society London, 143, 607–618.

Bearth, P., 1967. Die ophiolite der Zone von Zermatt-Saas Fee. Beitrage Geologische Karte Schweitz, 132, 1–130.

Bearth, P., 1976. Zur Gliederung der Bündnerschiefer in der Region von Zermatt. Eclogae Geologicae Helvetiae, 69, 149–161.

Beccaluva, L., Dal Piaz, G.V. & Macciotta, G., 1984. Transitional to normal MORB ophiolitic metabasites from the Zermatt-Saas, Combin and Antrona units, western Alps: implications for the paleogeografic evolution of the western Tethyan basin. Geologie en Mijnbouw, 63, 165–177.

Bortolami, G. & Dal Piaz, G.V., 1968. I filoni di gabbri rodingitici di Givoletto e Casellette nel massiccio ultrabasico di Lanzo (Torino). Bollettino della Societa Geologica Italiana, 87, 479–490.

Bucher, K. & Grapes, R., 2009. The eclogite-facies Allalin gabbro of the Zermatt-Saas ophiolite, Western Alps: a record of subduction zone hydration. Journal of Petrology, 50, 1405–1442.

Bucher, K., Fazis, Y., de Capitani, C. & Grapes, R., 2005. Blueschists, eclogites, and decompression assemblages of the Zermatt-Saas ophiolite: high-pressure metamorphism of subducted Tethys lithosphere. American Mineralogist, 90, 821–835.

Caron, J.M., Polino, R., Pognante, U. et al., 1984. Ou sont les sutures majeures dans les Alpes internes? (transversale Briançon-Torino). Memorie della Societa Geologica Italiana, 29, 71–78.

Cartwright, I. & Barnicoat, A.C., 2002. Petrology, geochronology, and tectonics of shear zones in the Zermatt-Saas and Combin zones of the Western Alps. Journal of Metamorphic Geology, 20, 263–281.

Castelli, D., Clerico, F. & Rossetti, P., 1995. Relict igneous relationships in the eclogitic meta-ophiolite complex of Colle Altare (Valli di Lanzo, Western Italian Alps). In: Studies of Metamorphic Rocks and Minerals of the Western Alps (ed. Lombardo, B.), Museo Regionale di Scienze Naturali, Torino, 13, 131–152.

Chinner, G.A. & Dixon, J.E., 1973. Some high pressure parageneses of the Allalin gabbro, Valais, Switzerland. Journal of Petrology, 14, 185–202.

Cloos, M., 1993. Lithospheric buoyancy and collisional orogenesis: subduction of oceanic plateaus, continental margins, island arcs, spreading ridges and seamounts. Geological Society of America Bulletin, 105, 715–737.

Coleman, R.G., 1967. Low-temperature reaction zones and alpine ultramafic rocks of California, Oregon and Washington. U.S. Geological Survey Bulletin, 1247, 1–49.

Dal Piaz, G.V., 1965. La formazione mesozoica dei calcescisti con pietre verdi fra la Valsesia e la Valtournanche ed i suoi rapporti strutturali con il ricoprimento del Monte Rosa e con la Zona Sesia-Lanzo. Bollettino della Societa Geologica Italiana, 84, 67–104.

Dal Piaz, G.V., 1967. Le "granatiti" (rodingiti L. S.) nelle serpentine delle Alpi Occidentali italiane. Memorie della Societa Geologica Italiana, 6, 267–313.

Dal Piaz, G.V., 1969. Filoni rodingitici e zone di reazione a bassa temperatura al contatto tettonico tra serpentine e rocce incassanti nelle Alpi occidentali italiane. Rendiconti della Societa Italiana di Mineralogia e Petrologia, 25, 263–316.

Dal Piaz, G.V., 1974. Le metamorphisme de haute pression et basse temperature dans l'evolution structurale du bassin ophiolitique alpino-apenninique. Schweizerische Mineralogische und Petrographische Mitteilungen, 54, 399–424.

Dal Piaz, G.V., 1999. The Austroalpine-Piedmont nappe stack and the puzzle of Alpine Tethys. In: 3rd Workshop on Alpine Geological Studies (eds Gosso, G., Jadoul, F., Sella, M. & Spalla, M.I.), Memorie di Scienze Geologiche, 51, 155–176.

Dal Piaz, G.V. & Ernst, W.G., 1978. Areal geology and petrology of eclogites and associated metabasites of the Piemonte ophiolite nappe, Breuil-St. Jacques area, Italian Western Alps. Tectonophysics, 51, 99–126.

Dal Piaz, G.V., Di Battistini, G., Gosso, G. & Venturelli, G., 1980. Rodingitic gabbro dykes and rodingitic reaction zones in the upper Valtournanche-Breuil area, Piemonte ophiolite nappe, Italian Western Alps. Archives des Sciences de Geneve, 33, 161–179.

Dal Piaz, G.V., Venturelli, G., Spadea, P. & Di Battistini, G., 1981. Geochemical features of metabasalts and metagabbros from the Piemonte ophiolite nappe, Italian Western Alps. Neues Jahrbuch für Mineralogie – Abhandlungen, 142, 248–269.

Dale, C.W., Burton, K.W., Pearson, D.G. et al., 2009. Highly siderophile element behaviour accompanying subduction of oceanic crust: whole rock and mineral-scale insights from a high-pressure terrain. Geochimica et Cosmochimica Acta, 73, 1394–1416.

De Giusti, F., Dal Piaz, G.V., Schiavo, A., Massironi, M., Monopoli, B. & Bistacchi, A., 2003. Carta geotettonica della Valle d'Aosta. Memorie Scienze Geologiche, 55, 129–149.

Diener, J.F.A., Powell, R., White, R.W. & Holland, T.J.B., 2007. A new thermodynamic model for clino- and orthoamphiboles in the system $Na_2O$–CaO–FeO–MgO–$Al_2O_3$–$SiO_2$–$H_2O$–O. Journal of Metamorphic Geology, 25, 631–656.

Dubińska, E., Bylina, P. & Kozłowsky, A., 2004. Garnets from lower Silesia rodingites: constraints from their chemistry. Polskie Towarzystwo Mineralogiczne – Prace Specjalne, 24, 135–139.

Ernst, W.G. & Dal Piaz, G.V., 1978. Mineral parageneses of eclogitic rocks and related mafic schists of the Piemonte ophiolite nappe, Breuil-St Jacques area, Italian Western Alps. American Mineralogist, 63, 621–640.

Ferrando, S., Frezzotti, M.L., Orione, P., Conte, R.C. & Compagnoni, R., 2010. Late-Alpine rodingitization in the Bellecombe meta-ophiolites (Aosta Valley, Italian Western Alps): evidence from mineral assemblages and serpentinization-derived $H_2$-bearing brine. International Geology Review, 52, 1220–1243.

Festa, A., Balestro, G., Dilek, Y. & Tartarotti, P., 2015. A Jurassic oceanic core complex in the high-pressure Monviso ophiolite (western Alps, NW Italy). Lithosphere, 7, 646–652.

Fontana, E., Panseri, M. & Tartarotti, P., 2008. Oceanic relict textures in the Mount Avic serpentinets, Western Alps. Ofioliti, 33, 105–118.

Fontana, E., Tartarotti, P., Panseri, M. & Buscemi, S., 2015. Geological map of the Mount Avic massif (Western Alps Ophiolites). Journal of Maps, 11, 126–135.

Frezzotti, M.L., Selverstone, J., Sharp, Z.D. & Compagnoni, R., 2011. Carbonate dissolution during subduction revealed by diamond-bearing rocks from the Alps. Nature Geoscience, 4, 703–706.

Frost, B.R., 1975. Contact metamorphism of serpentinite, chloritic blackwall and rodingite at Paddy-Go-Easy Pass, Central Cascades, Washington. Journal of Petrology, 16, 272–313.

Frost, B.R., Beard, J.S., McCaig, A. & Condliffe, E., 2008. The formation of micro-rodingites from IODP Hole U1309D: key to understanding the process of serpentinization. Journal of Petrology, 49, 1579–1588.

Giacometti, F., Evans, K.A., Rebay, G. et al., 2014. Sulfur isotope evolution in sulfide ores from Western Alps: assessing the influence of subduction-related metamorphism. Geochemistry, Geophysics, Geosystems, 15, 3808–3829.

Gnos, E. & Armbruster, T., 2006. Relationship among metamorphic grade, vesuvianite "rod polytypism", and vesuvianite composition. American Mineralogist, 91, 862–870.

Gosso, G., Rebay, G., Roda, M. et al., 2015. Taking advantage of petrostructural heterogeneities in subduction-collisional orogens, and effect on the scale of analysis. In: Progresses in Deciphering Structures and Compositions of Basement Rocks (eds Fazio, E., Fiannacca, P., Ortolano, G., Punturo, R., Zanoni, D. & Zucali, M.), Periodico di Mineralogia, 84, 779–825.

Gouzu, C., Itaya, T., Hyodo, H. & Matsuda, T., 2006. Excess $^{40}$Ar-free phengite in ultrahigh-pressure metamorphic rocks from the Lago di Cignana area, Western Alps. Lithos, 92, 418–430.

Green, E.C.R., Holland, T.J.B. & Powell, R., 2007. An order–disorder model for omphacitic pyroxenes in the system jadeite–diopside–hedenbergite–acmite, with applications to eclogite rocks. American Mineralogist, 92, 1181–1189.

Groppo, C., Beltrando, M. & Compagnoni, R., 2009. The P-T path of the ultra-high pressure Lago Di Cignana and adjoining high-pressure meta-ophiolitic units: insights into the evolution of the subducting Tethyan slab. Journal of Metamorphic Geology, 27, 207–231.

Guiraud, M., Powell, R. & Rebay, G., 2001. $H_2O$ in metamorphism and unexpected behaviour in the preservation of metamorphic assemblages. Journal of Metamorphic Geology, 19, 445–454.

Handy, M.R., Schmid, S.M., Bousquet, R., Kissling, E. & Bernoulli, D., 2010. Reconciling plate-tectonic reconstructions of Alpine Tethys with the geological–geophysical record of spreading and subduction in the Alps. Earth-Science Reviews, 102, 121–158.

Hey, M.H., 1954. A new review of the chlorites. Mineralogical Magazine, 30, 277–292.

Hobbs, B.E., Ord, A., Spalla, M.I., Gosso, G. & Zucali, M., 2010. The interaction of deformation and metamorphic reactions. In: Advances in Interpretation of Geological Processes: Refinement of Multi-scale Data and Integration in Numerical Modelling (eds Spalla, M.I., Marotta, A.M. & Gosso, G.), Geological Society of London Special Publications, 332, 189–222.

Hoisch, T.D., 1985. The solid solution chemistry of vesuvianite. Contributions to Mineralogy and Petrology, 89, 205–214.

Holland, T.J.B. & Powell, R., 1998. An internally consistent thermodynamic data set for phases of petrological interest. Journal of Metamorphic Geology, 16, 309–344.

Holland, T.J.B., Baker, J.M. & Powell, R., 1998. Mixing properties and activity – composition relationships of chlorites in the system MgO-FeO-$Al_2O_3$-$SiO_2$-$H_2O$. European Journal of Mineralogy, 10, 395–406.

Honnorez, J. & Kirst, P., 1975. Petrology of rodingites from the equatorial Mid-Atlantic fracture zones and their geotectonic significance. Contributions to Mineralogy and Petrology, 49, 233–257.

Ito, J. & Arem, J.E., 1970. Idocrase: synthesis, phase relations and crystal chemistry. American Mineralogist, 55, 880–921.

van der Klauw, S.N.G.C., Reinecke, T. & Stöckhert, B., 1997. Exhumation of ultrahigh-pressure metamorphic oceanic crust from Lago di Cignana, Piemontese zone, Western Alps. Lithos, 41, 79–102.

Kobayashi, S. & Kaneda, H., 2010. Rodingite with Ti- and Cr-rich vesuvianite from Sartuohai chromium deposit, Xinjiang, China. Journal of Mineralogical and Petrological Sciences, 105, 112–122.

Lagabrielle, Y., Vitale Brovarone, A. & Ildefonse, B., 2015. Fossil oceanic core complexes recognized in the blueschist metaophiolites of Western Alps and Corsica. Earth-Science Reviews, 141, 1–26.

Lapen, T.J., Johnson, C.M., Baumgartner, L.P., Mahlen, N.J., Beard, B.L. & Amato, J.M., 2003. Burial rates during prograde metamorphism of an ultrahigh pressure terrane: an example from Lago di Cignaga, western Alps, Italy. Earth and Planetary Science Letters, 215, 57–72.

Lardeaux, J.M., 2014. Deciphering orogeny: a metamorphic perspective. Examples from European Alpine and Variscan belts Part I: Alpine metamorphism in the western Alps. A review. Bulletin de la Société Géologique de France, 185, 93–114.

Li, X.P., Rahn, M. & Bucher, K., 2004a. Metamorphic processes in rodingites of the Zermatt-Saas ophiolite. International Geology Review, 46, 28–51.

Li, X.P., Rahn, M. & Bucher, K., 2004b. Serpentinites of the Zermatt-Saas ophiolite complex and their texture evolution. Journal of Metamorphic Geology, 22, 159–177.

Li, X.P., Zhang, L., Wei, C., Ai, Y. & Chen, J., 2007. Petrology of rodingite derived from eclogite in western Tianshan, China. Journal of Metamorphic Geology, 25, 363–382.

Li, X.P., Rahn, M. & Bucher, K., 2008. Eclogite facies metarodingites – phase relations in the system $SiO_2$-$Al_2O_3$-$Fe_2O_3$-FeO-MgO-CaO-$CO_2$-$H_2O$: an example from the Zermatt-Saas ophiolite. Journal of Metamorphic Geology, 26, 347–364.

Mahlen, N.J., Baumgartner, L.P. & Beard, B.L., 2005. Provenance of Jurassic Tethyan sediments in the HP/UHP Zermatt-Saas ophiolite, western Alps. Geological Society of America Bulletin, 117, 530–544.

Martin, S. & Tartarotti, P., 1989. Polyphase HP metamorphism in the ophiolitic glaucophanites of the lower St. Marcel valley (Aosta, Italy). Ofioliti, 14, 135–156.

Martin, S., Tartarotti, P. & Dal Piaz, G.V., 1994. The Mesozoic ophiolites of the Alps: a review. Bollettino di Geofisica Teorica ed Applicata, 36, 175–219.

Martin, S., Rebay, G., Kienast, J.R. & Mevel, C., 2008. An ophiolitic palaeo-hydrothermal field metamorphosed in the eclogite-facies from the Italian western Alps, Saint Marcel valley. Ofioliti, 33, 49–63.

McNamara, D.D., Wheeler, J., Pearce, M. & Prior, D.J., 2012. Fabrics produced mimetically during static metamorphism in retrogressed eclogites from the Zermatt-Saas zone, Western Italian Alps. Journal of Structural Geology, 44, 167–178.

de Meyer, C.M.C., Baumgartner, L.P., Beard, B.L. & Johnson, C.M., 2014. Rb–Sr ages from phengite inclusions in garnets from high pressure rocks of the Swiss Western Alps. Earth and Planetary Science Letters, 395, 205–216.

Mogessie, A. & Rammlamair, D., 1994. Occurrence of zoned uvarovite-grossular garnet in a rodingite from the Vumba Schist Belt, Botswana, Africa: implications for the origin of rodingites. Mineralogical Magazine, 58, 375–386.

Morimoto, N., 1988. Nomenclature of pyroxenes. Mineralogical Magazine, 52, 535–550.

Nicolas, A., 1966. Etude pétrochimique des Roches vertes et de leurs minéraux entre Dora Maïra et Grand Paradis. Le complexe Ophiolites-Schistes lustrés entre Dora Maïra et Grand Paradis. Tectonique et métamorphisme. Thèse d'État, Nantes, 299 pp.

Nyunt, T.T., Theye, T. & Massonne, H.-J., 2009. Na-rich vesuvianite in jadeitite of the Tawmaw jade district, northern Myanmar. Periodico di Mineralogia, 78, 5–18.

O'Hanley, D.S., Schandl, E.S. & Wicks, F.J., 1992. The origin of rodingites from Cassiar, British Columbia, and their use to estimate T and P($H_2O$) during serpentinization. Geochimica et Cosmochimica Acta, 56, 97–108.

Palandri, J.L. & Reed, M.H., 2004. Geochemical models of metasomatism in ultramafic systems: serpentinization, rodingitization, and sea floor carbonate chimney precipitation. Geochimica et Cosmochimica Acta, 68, 1115–1133.

Panseri, M., Fontana, E. & Tartarotti, P., 2008. Evolution of rodingitic dykes: metasomatism and metamorphism in the Mount Avic serpentinites (Alpine ophiolites, Southern Aosta Valley). Ofioliti, 33, 165–185.

Passchier, C.W. & Trouw, R.A.J., 2005. Microtectonics. Springer, Berlin, Heidelberg, New York.

Pfeiffer, H.R., Colombi, A. & Ganguin, J., 1989. Zermatt-Saas and Antrona Zone: a petrogenetic and geochemical comparison of polyphase metamorphic ophiolites of the Western-Central Alps. Schweizerische Mineralogische und Petrographische Mitteilungen, 69, 217–236.

Piccardo, G.B., Messiga, B. & Cimmino, F., 1980. Antigoritic serpentinites and rodingites of the Voltri Massif: some petrological evidences for their evolutive history. Ofioliti, 5, 111–114.

Pitcher, W.S. & Flinn, G.W. (eds), 1965. Controls of Metamorphism. A Symposium Under the Auspices of the Liverpool Geological Society. Oliver & Boyd, Edinburgh, London.

Pleuger, J., Roller, S., Walter, J.M., Jansen, E. & Froitzheim, N., 2007. Structural evolution of the contact between two Penninic nappes (Zermatt-Saas zone and Combin zone, Western Alps) and implications for the exhumation mechanism and palaeogeography. International Journal of Earth Sciences, 96, 229–252.

Polino, R., Dal Piaz, G.V. & Gosso, G., 1990. Tectonic erosion at the Adria margin and accretionary processes for the Cretaceous orogeny of the Alps. Mémoires de la Société géologique de France, 156, 345–367.

Powell, R., Holland, T.J.B. & Worley, B., 1998. Calculating phase diagrams involving solid solutions via non-linear equations with example using THERMOCALC. Journal of Metamorphic Geology, 16, 577–588.

Puga, E., Nieto, J.M., Díaz de Federico, A., Bodinier, J.L. & Morten, L., 1999. Petrology and metamorphic evolution of ultramafic rocks and dolerite dykes of the Betic Ophiolitic Association (Mulhacén Complex, SE Spain): evidence of eo-Alpine subduction following an ocean-floor metasomatic process. Lithos, 49, 23–56.

Rahn, M. & Bucher, K., 1998. Titanian clinohumite formation in the Zermatt-Saas ophiolites, Central Alps. Mineralogy and Petrology, 64, 1–13.

Rebay, G., Powell, R. & Diener, J.F.A., 2010. Calculated phase equilibria for a MORB composition in a P-T range, 450–650 C and 18–28 kbar: the stability of eclogite. Journal of Metamorphic Geology, 28, 635–645.

Rebay, G., Spalla, M.I. & Zanoni, D., 2012. Interaction of deformation and metamorphism during subduction and exhumation of hydrated oceanic mantle: insights from the Western Alps. Journal of Metamorphic Geology, 30, 687–702.

Reddy, S.M., Wheeler, J. & Cliff, R.A., 1999. The geometry and timing of orogenic extension: an example from the Western Italian Alps. Journal of Metamorphic Geology, 17, 573–589.

Regorda, A., Marotta, A.M. & Spalla, M.I., 2013. Numerical model of an ocean/continent subduction and comparison with Variscan orogeny natural data. Rendiconti Online della Società Geologica Italiana, 29, 142–145.

Reinecke, T., 1991. Very high pressure metamorphism and uplift of coesite-bearing metasediments from the Zermatt-Saas Zone, Western Alps. European Journal of Mineralogy, 10, 7–17.

Reinecke, T., 1998. Prograde high- to ultrahigh-pressure metamorphism and exhumation of oceanic sediments at Lago di

Cignana, Zermatt-Saas Zone, Western Alps. Lithos, 42, 147–189.

Rice, J.M., 1983. Metamorphism of rodingites: part I. Phase relations in a portion of the system CaO-MgO-$Al_2O_3$-$SiO_2$-$CO_2$-$H_2O$. American Journal of Science, 283, 121–150.

Ring, U., 1995. Horizontal contraction or horizontal extension? Heterogeneous late Eocene and early Oligocene general shearing during blueschist and greenschist facies metamorphism at the Pennine-Austroalpine boundary zone in the Western Alps. Geologische Rundschau, 84, 843–859.

Roda, M., Spalla, M.I. & Marotta, A.M., 2012. Integration of natural data within a numerical model of ablative subduction: a possible interpretation for the Alpine dynamics of the Austroalpine crust. Journal of Metamorphic Geology, 30, 973–996.

Rösli, U., Hoernes, S. & Köppel, V., 1991. Isotope data of metarodingites and associated rocks from the Lanzo and Bracco ophiolitic massif: indication on the evolution of the Alpino-type ultramafic-mafic complexes. Schweizerische Mineralogische und Petrographische Mitteilungen, 71, 125–141.

Rossman, G.R. & Aines, R.D., 1991. The hydrous components in garnets: grossular-hydrogrossular. American Mineralogist, 76, 1153–1164.

Rubatto, D., 1998. Dating of pre-Alpine magmatism, Jurassic ophiolites and Alpine subductions in the Western Alps. PhD, Swiss Federal Institute of Technology, Zurich, 174 pp.

Rubatto, D., Gebauer, D. & Fanning, M., 1998. Jurassic formation and Eocene subduction of the Zermatt-Saas-Fee ophiolites: implications for the geodynamic evolution of the Central and Western Alps. Contributions to Mineralogy and Petrology, 132, 269–287.

Scambelluri, M. & Rampone, E., 1999. Mg-metasomatism of oceanic gabbros and its control on Ti-clinohumite formation during eclogitization. Contributions to Mineralogy and Petrology, 135, 1–17.

Schandl, E.S., O'Hanley, D.S. & Wicks, F.J., 1989. Rodingites in serpentinized ultramafic rocks of the Abitibi greenstone belt, Ontario. Canadian Mineralogist, 27, 579–591.

Skora, S., Lapen, T.J., Baumgartner, L.P., Johnson, C.M., Hellebrand, E. & Mahlen, N.J., 2009. The duration of prograde garnet crystallization in the UHP eclogites at Lago di Cignana, Italy. Earth and Planetary Science Letters, 287, 402–411.

Skora, S., Mahlen, N.J., Johnson, C.M. et al., 2015. Evidence for protracted prograde metamorphism followed by rapid exhumation of the Zermatt-Saas Fee ophiolite. Journal of Metamorphic Geology, 33, 711–734.

Spalla, M.I. & Marotta, A.M., 2007. P-T evolutions vs. numerical modeling: a key to unravel the Paleozoic to Early-Mesozoic tectonic evolution of the Alpine area. Periodico di Mineralogia, 76, 267–308.

Spalla, M.I., Zucali, M., di Paola, S. & Gosso, G., 2005. A critical assessment of the tectono-thermal memory of rocks and definition of the tectono-metamorphic units: evidence from fabric and degree of metamorphic transformations. In: Deformation Mechanisms, Rheology and Tectonics: From Minerals to the Lithosphere (eds Gapais, D., Brun, J.P. & Cobbold, P.R.), Geological Society, London, Special Publications, 243, 227–247.

Spalla, M.I., Gosso, G., Marotta, A.M., Zucali, M. & Salvi, F., 2010. Analysis of natural tectonic systems coupled with numerical modelling of the polycyclic continental lithosphere of the Alps. International Geology Review, 52, 1268–1302.

Spear, F.S., 1993. Metamorphic Phase Equilibria and Pressure-Temperature-Time Paths. BookCrafters Inc, Chelsea, MI.

Springer, K., Lapen, T.J., Baumgartner, L.P., Johnson, C.M. & Beard, B.L., 2009. Sm-Nd geochronology of the Zermatt-Saas ophiolite, northern Italy. Goldsmith Conference. P. A1258.

Tsikouras, B., Karipi, S., Rigopoulos, I., Perraki, M., Pomonis, P. & Hatzipanagiotou, K., 2009. Geochemical processes and petrogenetic evolution of rodingite dykes in the ophiolite complex of Othrys (Central Greece). Lithos, 113, 540–554.

Tumiati, S., Martin, S. & Godard, G., 2010. Hydrothermal origin of manganese in the high-pressure ophiolite metasediments of Praborna ore deposit (Aosta Valley, Western Alps). European Journal of Mineralogy, 22, 577–594.

Turner, F.J. & Weiss, L.E., 1963. Structural Analysis of Metamorphic Tectonites. MacGraw-Hill, New York, NY.

Valley, J.W., Peacor, D., Bowman, J.R., Essene, E.J. & Allard, M.J., 1985. Crystal chemistry of a Mg-vesuvianite and implications for phase equilibria in the system CaO-MgO-$Al_2O_3$-$SiO_2$-$H_2O$-$CO_2$. Journal of Metamorphic Geology, 3, 137–153.

Vernon, R.H., 2004. A Practical Guide to Rock Microstructure. Cambridge University Press, Cambridge.

Wassmann, S., Stöckhert, B. & Trepmann, C.A., 2011. Dissolution precipitation creep versus crystalline plasticity in high-pressure metamorphic serpentinites. Geological Society of London, 360, 129–149.

Weber, S., Sandmann, S., Miladinova, I. et al., 2015. Dating the initiation of Piemonte-Liguria Ocean subduction: Lu–Hf garnet chronometry of eclogites from the Theodul Glacier Unit (Zermatt-Saas zone, Switzerland). Swiss Journal of Geosciences, 108, 183–199.

White, R.W., Powell, R. & Holland, T.J.B., 2007. Progress relating to calculation of partial melting equilibria for metapelites. Journal of Metamorphic Geology, 25, 511–527.

Whitney, D.L. & Evans, B.W., 2010. Abbreviations for names of rock-forming minerals. American Mineralogist, 95, 185–187.

Williams, P.F., 1985. Multiply deformed terrains – problems of correlation. Journal of Structural Geology, 7, 269–280.

Zanoni, D., Rebay, G., Bernardoni, J. & Spalla, M.I., 2012. Using multiscale structural analysis to infer high-/ultrahigh-pressure assemblages in subducted rodingites of the Zermatt-Saas Zone at Valtournanche, Italy. Journal of the Virtual Explorer, 41, 2–30. paper 6.

Received 29 September 2015; revision accepted 28 July 2016.